


# A scheme for radiation pressure and photon diffusion with the M1 closure in RAMSES-RT

J. Rosdahl<sup>1</sup> and R. Teyssier<sup>2</sup>

<sup>1</sup>*Leiden Observatory, Leiden University, PO Box 9513, NL-2300 RA Leiden, the Netherlands*

<sup>2</sup>*Institute for Computational Science, University of Zürich, Winterthurerstrasse 190, CH-8057 Zürich, Switzerland*

Accepted 2015 March 7. Received 2015 February 13; in original form 2014 November 24

## ABSTRACT

We describe and test an updated version of radiation-hydrodynamics in the RAMSES code, that includes three new features: (i) radiation pressure on gas, (ii) accurate treatment of radiation diffusion in an unresolved optically thick medium, and (iii) relativistic corrections that account for Doppler effects and work done by the radiation to first order in  $v/c$ . We validate the implementation in a series of tests, which include a morphological assessment of the M1 closure for the Eddington tensor in an astronomically relevant setting, dust absorption in an optically semithick medium, direct pressure on gas from ionizing radiation, convergence of our radiation diffusion scheme towards resolved optical depths, correct diffusion of a radiation flash and a constant luminosity radiation, and finally, an experiment from Davis et al. of the competition between gravity and radiation pressure in a dusty atmosphere, and the formation of radiative Rayleigh–Taylor instabilities. With the new features, RAMSES-RT can be used for state-of-the-art simulations of radiation feedback from first principles, on galactic and cosmological scales, including not only direct radiation pressure from ionizing photons, but also indirect pressure via dust from multiscattered IR photons reprocessed from higher-energy radiation, both in the optically thin and thick limits.

**Key words:** radiative transfer – methods: numerical.

## 1 INTRODUCTION

Recent years have seen great advances in the theory of galaxy evolution, in part thanks to the insight gained from hydrodynamical simulations. Among the clearest messages to come out of the simulations is the necessity for feedback to regulate galaxy evolution. Without it, the galaxies are too massive and compact compared to observations (e.g. Sugihara & Ostriker 1998; Balogh et al. 2001). While the inclusion of feedback from supernovae (SN) and active galactic nuclei (AGN) has helped to relieve this so-called overcooling problem, overcompact galaxies remain an issue in cosmological simulations (Scannapieco et al. 2012, though see Schaye et al. 2015). This can partly be traced directly to numerical overcooling, due to the lack of resolution and/or the details of the hydrodynamical solver (e.g. Creasey et al. 2011; Dalla Vecchia & Schaye 2012; Keller et al. 2014).

Part of the problem may also be the lack of alternative feedback mechanisms in simulations, such as cosmic rays (e.g. Pfrommer et al. 2007; Booth et al. 2013; Hanaasz et al. 2013; Salem & Bryan 2014), or radiation (e.g. Gayley, Owocki & Cranmer 1995; Murray, Quataert & Thompson 2005; Krumholz & Matzner 2009).

Radiation feedback in particular has been employed in a number of recent simulation works to improve galaxy evolution models and quench star formation rates (e.g. Oppenheimer & Davé 2006; Brook et al. 2012; Agertz & Kravtsov 2014; Hopkins et al. 2014). However, even if those simulations are successful in reproducing a set of observations, it remains unclear and debated whether radiation feedback is effective, and how it works in detail.

Radiation typically *heats* the gas it interacts with, and though the heating is relatively gentle compared to AGN and SN feedback, it may well give an important boost to those other feedback mechanisms (e.g. Pawlik & Schaye 2009). *Radiation pressure* may also be an important feedback mechanism on its own, stirring up the gas in the interstellar medium (ISM) and even generating outflows. Here, *direct pressure* from ionizing radiation can play a role (e.g. Haehnelt 1995; Wise et al. 2012; Ceverino et al. 2014), although recent works have relied more on the boost in radiation pressure that can be gained by reprocessed *multiscattered* infrared (IR) radiation, which could in particular be a major feedback mechanism in optically thick ultraluminous IR galaxies, or ULIRGS (e.g. Murray, Quataert & Thompson 2010; Thompson et al. 2015). This last mentioned multiscattering feedback mechanism in particular has been under debate in the recent literature. Observationally there is not a lot of evidence for radiation feedback from star formation, though recent observations of stellar nurseries hint that its effect on the ISM

\*E-mail: jokirosdahl@gmail.com

is mild and mostly in the form of heating (Lopez et al. 2014). It is likely though that the nature of the radiation feedback mechanism depends heavily on the environment, mainly the optical thickness of the galactic gas.

It does not help that most simulations that invoke some form of radiation feedback do so with pure hydrodynamics (HD), using subgrid models and approximations instead of the radiation-hydrodynamics (RHD) needed to model radiation feedback from first principles.

This is understandable, as radiative transfer (RT) is both complex and costly due to the usually much shorter inherent time-scales and large number of computational dimensions. RHD is still young compared to the more mature field of HD in galaxy evolution, but in the last decade or so, increased computational power and the development of new approaches and algorithms has finally made RHD a feasible prospect in astronomical and cosmological simulations (e.g. Petkova & Springel 2009; Krumholz, Klein & McKee 2011; Pawlik & Schaye 2011; Wise & Abel 2011; Jiang, Stone & Davis 2012; Skinner & Ostriker 2013; Norman et al. 2015).

Recently, in Rosdahl et al. (2013, hereafter R13), we presented an implementation of RHD in the cosmological code RAMSES (Teyssier 2002), that we call RAMSES-RT. This work focused on ionizing radiation and its interaction with hydrogen and helium via ionization heating, which is indeed one of the possibly relevant physical mechanisms in radiation feedback. However, we still neglected radiation pressure in that work, which is cited by many of the aforementioned works as being the main ‘culprit’ in radiation feedback.

In this paper, we describe a step towards simulating radiation feedback in galaxy evolution simulations from first principles, with the additions to RAMSES-RT of radiation pressure and reprocessed dust-coupled multiscattered radiation. Our new features include a novel approach to modelling IR radiation *trapping*, that describes accurately both the optically thin and thick regimes, a feature that does not come naturally in RT implementations, which usually work well in one regime but not the other.

This paper is split into two main sections, describing the method details (Section 2) and then verification tests (Section 3). In the methods section, we begin in Section 2.1 by presenting the basic moment RHD equations to be solved, focusing on the new aspects of the radiation force and radiation-dust coupling in the optically thick regime. Then, in Section 2.2, we recall the main ingredients of our existing RHD solver, and in Section 2.3 we detail the addition of the radiation pressure and IR–dust interaction. Concluding the methods section, we present in Section 2.4 our innovative approach to modelling the propagation of IR radiation correctly in *both* the optically thin and thick limits. The rest of the paper is dedicated to tests of our implementation, starting with qualitative tests of radiation field morphology in the optically thin and thick limits (Sections 3.1 and 3.2), going on to test the direct momentum transfer from photons to gas (Section 3.3), the correct diffusion of radiation in the optically thick limit (Sections 3.4–3.6), and, finally, comparing our code directly to another RHD implementation in a previously published experiment of the competition between radiation pressure and gravity, for which most of our new additions are quite relevant (Section 3.7). In the appendix we describe relativistic corrections to our implementation, the details of which are omitted from the main text for clarity.

## 2 METHODS

RHD has been partially implemented in RAMSES-RT (R13), which is an extension of the adaptive mesh refinement (AMR) code RAMSES

(Teyssier 2002). RAMSES models the interaction of dark matter, stellar populations, and baryonic gas, via gravity, HD, and radiative cooling. The gas evolution is computed using a second-order Godunov scheme for the Euler equations, while trajectories of collisionless DM and stellar particles are computed using a particle-mesh solver. RAMSES-RT adds the propagation of photons and their interaction with gas via photoionization and heating of hydrogen and helium. The advection of photons between grid cells is described with the moment method and the M1 closure relation for the Eddington tensor. RAMSES-RT solves the non-equilibrium evolution of the ionization fractions of hydrogen and helium, along with ionizing photon fluxes and the temperature in each grid cell.

The goal of the present paper is to extend the RHD implementation in RAMSES, adding three important features: (i) we now include the radiative force, which couples the radiation flux to the gas momentum equation; (ii) we introduce a new scheme to recover the proper asymptotic limit in the radiation diffusion regime, in case the mean free path is much smaller than the grid spacing; (iii) we add relativistic corrections to the RHD equations, accounting for Doppler effects up to first order in  $v/c$ , where  $v$  and  $c$  are the gas and light speeds, respectively, and for the work done by the radiation force on the gas. In this section, we will review the main characteristics of the RAMSES-RT solver before discussing our new numerical scheme for the radiation force and for the preservation of the asymptotic diffusion regime. We will omit the order  $v/c$  relativistic corrections, which will be described in more detail in the appendix.

### 2.1 The RHD equations

We describe here the moment equations solved in RAMSES-RT, outlining the role played by the radiation force.

As detailed in R13, we use an important approximation to speed up our explicit scheme for radiation advection, where the time-step scales inversely with the speed of light  $c$ . In this so-called reduced speed of light approximation, we simply decrease the speed of light, typically by 1–3 orders of magnitude.<sup>1</sup> In this paper, we thus make an important distinction between  $c$ , the actual speed of light, and  $\tilde{c}$ , the reduced speed of light.

The starting point in deriving the RHD equations is the radiation specific intensity  $I_\nu(\mathbf{x}, \mathbf{n}, t)$ , describing the radiation flow (CGS units of  $\text{erg cm}^{-2} \text{s}^{-1} \text{Hz}^{-1} \text{rad}^{-2}$ ), over the dimensions of frequency  $\nu$ , location  $\mathbf{x}$ , unit direction  $\mathbf{n}$ , and time  $t$ . The evolution of the specific intensity is described by the RT equation:

$$\frac{1}{\tilde{c}} \frac{\partial I_\nu}{\partial t} + \mathbf{n} \cdot \nabla I_\nu = \eta_\nu - \kappa_\nu \rho I_\nu, \quad (1)$$

where  $\kappa_\nu$  is the gas opacity, ( $\text{cm}^2 \text{g}^{-1}$ ),  $\rho$  the gas density ( $\text{g cm}^{-3}$ ), and  $\eta_\nu$  the plasma emissivity ( $\text{erg s}^{-1} \text{cm}^{-3} \text{Hz}^{-1} \text{rad}^{-2}$ , usually assumed to be isotropic).

We define the radiation energy density  $E$  ( $\text{erg cm}^{-3}$ ), the radiation flux  $\mathbf{F}$  ( $\text{erg cm}^{-2} \text{s}^{-1}$ ), and the radiation pressure  $\mathbf{P}$  ( $\text{erg cm}^{-3}$ ), in a group of photons over a specified frequency range, as *moments*

<sup>1</sup> This approximation is valid only if the modified light crossing time is still short compared to the sound crossing time, the recombination time, and the advection time in the flow. If this is not the case, then the reduced speed of light approximation is invalid and one has to rely on either RT subcycles (Aubert & Teyssier 2008) or implicit time integration (Commerçon, Debout & Teyssier 2014).

<sup>2</sup> We will use CGS units (centimetres–grams–seconds) to clarify variable dimensions, but these are obviously interchangeable for other units systems.

(i.e. averages) of the radiation intensity over solid angle  $\Omega$  and frequency:

$$E(\mathbf{x}, t) = \frac{1}{\bar{c}} \int_{\nu} \int_{4\pi} I_{\nu}(\mathbf{x}, \mathbf{n}, t) d\nu d\Omega, \quad (2)$$

$$\mathbf{F}(\mathbf{x}, t) = \int_{\nu} \int_{4\pi} I_{\nu}(\mathbf{x}, \mathbf{n}, t) \mathbf{n} d\nu d\Omega, \quad (3)$$

$$\mathbf{P}(\mathbf{x}, t) = \frac{1}{\bar{c}} \int_{\nu} \int_{4\pi} I_{\nu}(\mathbf{x}, \mathbf{n}, t) \mathbf{n} \otimes \mathbf{n} d\nu d\Omega, \quad (4)$$

where  $\otimes$  denotes the outer product. Taking the zeroth and first moments of equation (1) and substituting the definitions (2)–(4) yields the well-known moment equations of radiation energy and flux (e.g. Mihalas & Mihalas 1984):

$$\frac{\partial E}{\partial t} + \nabla \cdot \mathbf{F} = S - \kappa_E \rho \bar{c} E, \quad (5)$$

$$\frac{1}{\bar{c}} \frac{\partial \mathbf{F}}{\partial t} + \bar{c} \nabla \cdot \mathbf{P} = -\kappa_F \rho \mathbf{F}, \quad (6)$$

where  $\kappa_E$  and  $\kappa_F$  are, respectively, the radiation energy and flux-weighted mean opacities, and the source function  $S$  is the integral of the emissivity over all solid angles and over the photon groups frequency range. With multiple photon groups, a separate set of moment equations exists for each group, which should in principle be denoted by photon group subscripts, i.e.  $E_i$ ,  $\mathbf{F}_i$ ,  $\mathbf{P}_i$ ,  $S_i$ ,  $\kappa_{E,i}$ , and  $\kappa_{F,i}$ . For the sake of simplicity, we omit those subscripts, unless they are required for clarification.

If the system under study is close to local thermodynamical equilibrium (LTE), where the gas emits as a blackbody, and the photon group covers a sufficiently large frequency range, the source function can be approximated by the frequency integral of a Planckian,

$$S = \kappa_P \rho c a T^4, \quad (7)$$

where  $a$  is the radiation constant,  $\kappa_P$  is the Planck mean opacity, and  $T$  is the gas temperature. This approximation is often used to describe the coupling between dust and IR radiation in the ISM (Mihalas & Mihalas 1984, chapter 6). We assume a *single-fluid* system in this work, where the gas and dust are also in LTE, i.e. at the same temperature. Note that in the previous equations, the opacities are computed in the *comoving* frame, moving with the gas, while the radiation moments are defined in the laboratory (or lab) frame. We ignore Doppler effects of these relative motions in the main text. However including them for non-relativistic flows introduces important additional terms which are described in the appendix.

If one assumes that the spectral energy distribution (SED) is close to a Planckian, then  $\kappa_E = \kappa_P$ . Another traditional approximation, when the fluid-radiation system is close to LTE and the optical depth is large, is to take  $\kappa_F \simeq \kappa_R$ , where the latter is the Rosseland mean. Under these approximations, valid only for systems close to LTE (such as for ISM dust and IR radiation), equations (5) and (6) simplify into

$$\frac{\partial E}{\partial t} + \nabla \cdot \mathbf{F} = \kappa_P \rho (c a T^4 - \bar{c} E), \quad (8)$$

$$\frac{\partial \mathbf{F}}{\partial t} + \bar{c}^2 \nabla \cdot \mathbf{P} = -\kappa_R \rho \bar{c} \mathbf{F}. \quad (9)$$

These equations are *not valid* in the optically thin regime and for systems far from LTE, such as for ionizing radiation coupled to the non-equilibrium chemistry of hydrogen and helium. Under such conditions, one can instead use a template spectrum, usually the

SED of stellar populations, to compute the average dust opacities (see R13).

The HD equations must be modified to account for the transfer of energy and momentum between radiation and gas. The fluid energy equation describes the evolution of the gas energy density

$$E_{\text{gas}} = \frac{1}{2} \rho v^2 + e, \quad (10)$$

where the right-hand side (RHS) terms are kinetic energy, with  $v$  the gas speed, and internal or ‘thermal’ energy  $e$ . Assuming LTE, the fluid energy equation becomes

$$\frac{\partial E_{\text{gas}}}{\partial t} + \nabla \cdot (\mathbf{v}(E_{\text{gas}} + P)) = \rho \mathbf{g} \cdot \mathbf{v} + \Lambda + \kappa_P \rho (\bar{c} E - c a T^4), \quad (11)$$

where  $\mathbf{v}$  and  $P$  are the gas velocity and pressure,  $\mathbf{g}$  is the local gravitational acceleration, and  $\Lambda$  represents cooling/heating via thermochemical processes (see R13). The new term here is the last one on the RHS, describing the internal energy exchange between the gas and the radiation field.

The fluid momentum equation becomes

$$\frac{\partial \rho \mathbf{v}}{\partial t} + \nabla \cdot (\rho \mathbf{v} \otimes \mathbf{v} + P \mathbf{I}) = \rho \mathbf{g} + \frac{\kappa_R \rho}{c} \mathbf{F}, \quad (12)$$

where  $\mathbf{I}$  is the identity matrix. Here the new term is again the last one on the RHS, describing the radiation momentum absorbed by the gas. Note that the work done by the radiation force is absent. These terms of order  $v/c$  are introduced in the appendix as a relativistic correction, but we omit them from the main text for the sake of simplicity.

## 2.2 The radiation solver

RAMSES-RT solves the radiation advection equations (8) and (9) using the M1 closure for the Eddington tensor, first introduced by Levermore (1984). In this approximation, the Eddington tensor, defined as  $\mathbf{D} = \mathbf{D}E$ , is given explicitly by a simple *local* relation

$$\mathbf{D} = \frac{1 - \chi}{2} \mathbf{I} + \frac{3\chi - 1}{2} \mathbf{n} \otimes \mathbf{n}, \quad (13)$$

where  $\mathbf{n} = \mathbf{F}/|\mathbf{F}|$  and  $\chi$  depends only on the reduced flux,

$$f = \frac{|\mathbf{F}|}{\bar{c} E}, \quad (14)$$

as

$$\chi(f) = \frac{3 + 4f^2}{5 + 2\sqrt{4 - 3f^2}}. \quad (15)$$

It is based on the assumption that the angular distribution of the radiation intensity can be approximated by a Lorentz-boosted Planckian, in the direction of the radiation flux. This approximation recovers the asymptotic limit of the diffusion regime, when  $f \ll 1$ , so that  $\chi \simeq 1/3$  and  $\mathbf{D} \simeq \mathbf{I}/3$ . It also describes well the free streaming of radiation from a single source, when  $f \simeq 1$ , so that  $\chi \simeq 1$  and  $\mathbf{D} \simeq \mathbf{n} \otimes \mathbf{n}$ . In the intermediate regime, or in the presence of multiple sources, this is only an approximation, and the model must therefore be compared to existing exact solutions to assess its range of validity (Aubert & Teyssier 2008, R13).

A very important consequence of the M1 closure is that the resulting system of conservation laws (ignoring the source terms) is hyperbolic, and can therefore be integrated numerically using a classical Godunov scheme (Aubert & Teyssier 2008), and an operator split approach, where the radiation variables  $E$  and  $\mathbf{F}$  in

each cell are modified first using a conservative and *explicit* update from their intercell fluxes, and the source terms are included in a second step using a local, *implicit*, subcycling thermochemistry module (Aubert & Teyssier 2008, R13).

Stability of the numerical integration for the transport step is ensured using proper upwinding to compute the numerical flux, using a *Riemann solver*. In this paper, we use the Global Lax Friedrich (GLF) Riemann solver<sup>3</sup> (see Aubert & Teyssier 2008, R13), for which the interface radiation flux is explicitly

$$\mathbf{F}_{1/2}(\mathbf{U}_L, \mathbf{U}_R) = \frac{\mathbf{F}_R + \mathbf{F}_L}{2} - \frac{\tilde{c}}{2}(E_R - E_L), \quad (16)$$

where  $\mathbf{U} = (\mathbf{F}, E)$  is a cell state, the ‘1/2’ subscript refers to the Godunov intercell state, that we use to perform the final conservative update of the radiation energy, and the subscripts ‘L’ and ‘R’ refer to the neighbouring left and right cells. A similar formula holds for the intercell Eddington tensor to conservatively update the radiation flux. The first term on the RHS of equation (16) is the average of the right and left cells radiation fluxes. This term alone would give a second-order but *unstable* solution. The second term on the RHS of equation (16) is proportional to the difference of the right and left cell radiation densities. This is the stabilizing term, also called the numerical diffusion term. Indeed, one can formally rewrite the numerical flux as

$$\mathbf{F}_{1/2} = \frac{\mathbf{F}_R + \mathbf{F}_L}{2} - \frac{\tilde{c}\Delta x}{2} \frac{\partial E}{\partial x}, \quad (17)$$

where  $\Delta x$  is the width of the cell. We now see explicitly the numerical diffusion coefficient as  $\nu_{\text{num}} = \tilde{c}\Delta x/2$ . We will use these numerical concepts in Section 2.4.

### 2.3 A new RHD solver

The microscopic processes that are already included in RAMSES-RT (see R13) are the non-equilibrium chemistry of hydrogen and helium coupled to the ionizing radiation. We now describe the new features in RAMSES-RT which can be used to model the coupling between dust and IR radiation, and to model the injection of momentum into the gas by the radiation flux.

#### 2.3.1 Modified moment RT equations, for IR and higher energy photons

In RAMSES-RT, we now make a distinction between the group of IR photons and all other, higher-energy, groups. The IR photons are assumed to cover the energy range of dust emission and to be in LTE with the dust particles, exchanging energy via absorption and re-emission. Other groups, however, span energies above the dust emission. These photons can be absorbed by the dust, as well as by hydrogen and helium via photoionization, but the dust-absorbed energy is re-emitted at lower (IR) energies. Thus, the IR photons

can be seen as ‘multiscattered’, while all other photons are ‘single scattered’.

For a group  $i \neq \text{IR}$  of non-IR photons, the moment RT equations, following from equations (5) and (6), are unchanged from what we presented in R13, save for new dust absorption terms:

$$\frac{\partial E_i}{\partial t} + \nabla \cdot \mathbf{F}_i = - \sum_j^{\text{H I, He I, He II}} n_j \sigma_{ij} \tilde{c} E_i + \dot{E}_i - \kappa_i \rho \tilde{c} E_i, \quad (18)$$

$$\frac{\partial \mathbf{F}_i}{\partial t} + \tilde{c}^2 \nabla \cdot \mathbf{P}_i = - \sum_j^{\text{H I, He I, He II}} n_j \sigma_{ij} \tilde{c} \mathbf{F}_i - \kappa_i \rho \tilde{c} \mathbf{F}_i. \quad (19)$$

Here we sum over the hydrogen and helium species  $j$  which absorb ionizing photons, with  $\sigma_{ij}$  denoting the ionization cross-section ( $\text{cm}^2$ ) between photon group  $i$  and ion species  $j$ , which is zero for non-ionizing photons.  $\dot{E}$  is the rate of emission from point sources (stars, AGN) and hydrogen/helium recombinations. The last terms in each equation represent dust absorption, which scales with the dust-opacity ( $\kappa_i$ ) and the gas density.

The dust-absorbed energy is re-emitted into the IR photon group, for which the RT equations are

$$\begin{aligned} \frac{\partial E_{\text{IR}}}{\partial t} + \nabla \cdot \mathbf{F}_{\text{IR}} &= \kappa_{\text{P}} \rho (caT^4 - \tilde{c} E_{\text{IR}}) + \dot{E}_{\text{IR}} \\ &+ \sum_i^{\text{other groups}} \kappa_i \rho \tilde{c} E_i, \end{aligned} \quad (20)$$

$$\frac{\partial \mathbf{F}_{\text{IR}}}{\partial t} + \tilde{c}^2 \nabla \cdot \mathbf{P}_{\text{IR}} = -\kappa_{\text{R}} \rho \tilde{c} \mathbf{F}_{\text{IR}}. \quad (21)$$

These equations are the same as the previous equations (18) and (19) for non-IR photons, except that (i) we omit photoionization/recombination terms (in  $\dot{E}_{\text{IR}}$ ), as these photons have subionizing energies, (ii) the negative dust absorption terms in the previous equations become additive terms here, representing dust re-emission into the IR group, and (iii) we have added the first RHS term, which describes the coupling between IR radiation density and the gas (dust) temperature.

A great deal of complex physics is encapsulated inside  $\kappa_i$ ,  $\kappa_{\text{R}}$ , and  $\kappa_{\text{P}}$ , which depend on temperature, the dust content, and the exact shape of the radiation spectrum. One can use existing models for temperature-dependent dust opacities (e.g. Draine & Li 2007), assuming that the dust content scales with metallicity, and include a cut-off at  $T \gtrsim 1000$  K to model dust sublimation. In this work, however, we consider only constant values for the photon opacities, except for Section 3.7, where we use simple temperature-dependent functions. Updating the opacities to more complex forms is a straightforward addition to the code, and often specific to the problem at hand and the level of detail one seeks to achieve. We defer those considerations to future works.

As described in detail in R13, the RT moment equations are solved, after the HD step, with an operator splitting approach, where we solve in sequence the advection terms and the source/sink terms over an RHD time-step, for all cells in a given refinement level. The advection is solved explicitly and the source/sink terms are solved quasi-implicitly, together with the gas temperature, using thermochemistry subcycling. The only non-trivial addition to the solver is the coupling term for the gas and radiation, i.e. the first term on the RHS of equation (20), which is described next.

<sup>3</sup> RAMSES-RT also offers the possibility to use the Harten–Lax–van Leer (HLL) intercell flux function, which is less diffusive than GLF, but also produces less spherically symmetric radiation from stars, as we showed in R13. Our method for radiation trapping in the optically thick limit, which we develop in this paper, is however only strictly compatible with GLF, so we do not include the HLL function in the current work. Since we prefer the GLF function over HLL, which produces asymmetric radiation around stellar sources, we do not have immediate plans to adopt radiation trapping for HLL.



### 2.3.2 IR–dust temperature coupling

Ignoring advection terms and other sources of photon absorption/emission and gas cooling/heating, which are described in R13, the coupling between the IR energy density,  $E_{\text{IR}}$ , and the gas internal energy density,  $e$ , follows from equations (8) and (11), respectively:

$$\frac{\partial E_{\text{IR}}}{\partial t} = \kappa_{\text{P}} \rho (caT^4 - \tilde{c}E_{\text{IR}}), \quad (22)$$

$$\frac{\partial e}{\partial t} = \kappa_{\text{P}} \rho (\tilde{c}E_{\text{IR}} - caT^4). \quad (23)$$

These equations are solved in each thermochemistry substep *after* the updates of radiation energy density and gas temperature via other terms of absorption, emission, heating, and cooling. Keeping in mind the strong coupling between radiation and temperature, we solve semi-implicitly using a linear approach. In this formulation, the change in the state vector  $\mathbf{U}_E \equiv (E_{\text{IR}}, e)$ , over the thermochemistry time-step of length  $\Delta t$ , is

$$\Delta \mathbf{U}_E = \dot{\mathbf{U}}_E \Delta t (\mathbf{I} - \mathbf{J} \Delta t)^{-1}, \quad (24)$$

where  $\dot{\mathbf{U}}_E$  is the RHS of equations (22) and (23), and  $\mathbf{J} = \frac{\partial \dot{\mathbf{U}}_E}{\partial \mathbf{U}_E}$  is the Jacobian matrix, each evaluated at the start of  $\Delta t$ .

Taking advantage of the symmetry of the problem ( $\Delta E_{\text{IR}} = -\Delta e$ ), the update over  $\Delta t$  is obtained by

$$\Delta E_{\text{IR}} = -\Delta e = \frac{caT^4 - \tilde{c}E_{\text{IR}}}{(\kappa_{\text{P}} \rho \Delta t)^{-1} + \tilde{c} + 4caT^3 C_V^{-1}}, \quad (25)$$

where  $C_V = \left(\frac{\partial e}{\partial T}\right)_V = \frac{\rho k_{\text{B}}}{m_{\text{p}} \mu (\gamma - 1)}$  is the heat capacity at constant volume,  $k_{\text{B}}$  the Boltzmann constant,  $\mu$  the average particle mass in units of the proton mass  $m_{\text{p}}$ , and  $\gamma$  is the ratio of specific heats.

After the update of temperature and IR energy via equation (25), we reapply the 10 per cent thermochemistry rule (R13): if either  $T$  or  $E_{\text{IR}}$  (or both) was changed by more than 10 per cent from the original value, the entire thermochemistry substep is repeated with half the time-step length.

### 2.3.3 Momentum transfer from photons to gas

In the framework of the RHD method, the fluid momentum equation is

$$\frac{\partial \rho \mathbf{v}}{\partial t} + \nabla \cdot (\rho \mathbf{v} \otimes \mathbf{v} + P \mathbf{I}) = \rho \mathbf{g} + \dot{\mathbf{p}}_{\gamma}. \quad (26)$$

This is the same as equation (12), but generalized to the total local momentum absorption rate, per unit volume, from all photon groups via all radiation interactions (not only radiation–dust interactions):

$$\dot{\mathbf{p}}_{\gamma} = \sum_i^{\text{groups}} \frac{\mathbf{F}_i}{c} \left( \kappa_i \rho + \sum_j^{\text{H I, He I, He II}} \sigma_{ij} n_j \right). \quad (27)$$

The momentum transfer is implemented with an operator split approach, adding to the gas momentum in each RHD step after the thermochemistry step. Since both photon fluxes and absorber densities may change substantially during the subcycling of the thermochemistry equations over a single RHD time-step,  $\Delta t_{\text{RHD}}$ , we collect the absorbed momentum density over the subcycles, whose subtime-steps are limited such as to change the evolved quantities only by a small fraction (10 per cent) per substep:

$$\Delta \mathbf{p}_{\gamma} = \sum_k \Delta t_k \sum_i^{\text{groups}} \frac{\mathbf{F}_{i,k+1}}{c} \left( \kappa_i \rho + \sum_j^{\text{H I, He I, He II}} \sigma_{ij} n_{j,k+1} \right). \quad (28)$$

Here the outermost sum is over the thermochemistry substeps (with  $\sum_k \Delta t_k = \Delta t_{\text{RHD}}$ ). At the end of the thermochemistry subcycling of a cell, the total absorbed photon momentum density vector  $\Delta \mathbf{p}_{\gamma}$  is added to the gas momentum, and the gas specific total energy is updated to reflect the change in kinetic energy.

In addition to the direct radiation pressure just described, radiation pressure from isotropic diffusive IR radiation is also implemented in RAMSES-RT, as we will discuss in the next subsection.

## 2.4 Preserving the asymptotic diffusion limit

The *diffusion limit* is reached when the optical depth of the LTE radiation becomes unresolved and the photons propagate in a random walk.<sup>4</sup> Then, since  $F \ll \tilde{c}E$ , we get for the Eddington tensor (equation 13)  $\mathbf{D} = \mathbf{I}/3$ . In this case, we reach the asymptotic regime where equation (9) reduces to a static form (see Mihalas & Mihalas 1984, section 80)<sup>5</sup>, giving

$$\mathbf{F} \simeq -\frac{\tilde{c} \lambda_{\text{R}}}{3} \nabla E, \quad (30)$$

where  $\lambda_{\text{R}} = (\kappa_{\text{R}} \rho)^{-1}$  is the mean free path. This equation expresses the fact that in this regime, radiation is a diffusive process, with diffusion coefficient  $\nu_{\text{rad}} = \tilde{c} \lambda_{\text{R}}/3$ . The previous derivation for our numerical scheme (see equation 16) explicitly demonstrates that in the diffusion limit, the numerical diffusion of our M1 solver dominates over the true radiation diffusion when

$$\nu_{\text{num}} > \nu_{\text{rad}} \quad \text{or} \quad 3\Delta x > 2\lambda_{\text{R}}. \quad (31)$$

This last inequality is likely to occur in optically thick regions, where the optical depth of the cell,  $\tau_{\text{c}} = \Delta x/\lambda_{\text{R}}$ , is larger than 1.

As discussed in Liu (1987) and Bouchut (2004), if the equation (31) inequality occurs, operator splitting is not valid anymore, as source terms become stiff compared to the hyperbolic transport terms. The numerical result becomes severely inaccurate: radiation propagates with an effective mean-free-path equal to the cell size, much larger than the true mean-free-path, manifesting in photons which travel much too fast through the volume, compared to equation (30).

One possibility to resolve the problem and recover the correct diffusion of photons is to exploit the AMR technique and refine the grid adaptively so that  $\Delta x$  always stays smaller than, say,  $\lambda_{\text{R}}/4$ . This is unfortunately not always possible in realistic astrophysical applications where the opacity can be a highly non-linear function of temperature and density.

We now propose two different techniques to modify our base scheme in order to preserve the asymptotic diffusion regime posed by equation (30): (i) a modification of the Godunov flux that takes into account the diffusion source term (Section 2.4.1), and (ii) the

<sup>4</sup> This section concerns only the IR photon group, since other groups are assumed to be single scattering.

<sup>5</sup> The ratio between the time-dependent and static flux terms in equation (9) is

$$\frac{\frac{\partial \mathbf{F}}{\partial t}}{\kappa_{\text{R}} \rho \tilde{c} \mathbf{F}} \sim \frac{\lambda_{\text{R}}}{\tilde{c} \Delta t} = \left( \frac{\lambda_{\text{R}}}{\Delta x} \right)^2, \quad (29)$$

where we use the fact that a travelled distance  $\Delta x$  requires  $(\Delta x/\lambda_{\text{R}})^2$  interactions in a random walk, and hence the time to travel this distance is  $\Delta t = \frac{\Delta x^2}{\tilde{c} \lambda_{\text{R}}}$ . If  $\lambda_{\text{R}} \ll \Delta x$ , the time-dependent flux term is thus negligible, and we can use the static diffusion form (equation 30).

addition of a new photon (sub) group that we call *trapped photons* (Section 2.4.2). As opposed to *streaming photons*, these new photons are strictly isotropic in angular space.

#### 2.4.1 Asymptote-preserving Godunov fluxes

Following the methodology presented in Berthon, Charrier & Dubroca (2007), it is possible to correct for the effect of radiation diffusion by explicitly taking into account the source terms in the Riemann solver. The Riemann solution becomes much more complicated (see Berthon et al. 2007), but can be approximated by a simple modification of the intercell flux (equation 16) as

$$\mathbf{F}_{1/2} = \mathbf{F}_{1/2}(\alpha_L \mathbf{U}_L, \alpha_R \mathbf{U}_R), \quad (32)$$

where Berthon et al. (2007) introduced the new function  $\alpha(\tau_c)$ , which is, in case one uses the GLF numerical flux,

$$\alpha(\tau_c) = \frac{1}{1 + \frac{3}{2}\tau_c}. \quad (33)$$

This function encodes the modification to the Riemann solver that accounts for the source terms. It satisfies

$$\begin{aligned} \alpha &\rightarrow 1 \text{ when } \tau_c \rightarrow 0, & \text{and} \\ \alpha &\rightarrow \frac{2}{3\tau_c} \text{ when } \tau_c \rightarrow +\infty. \end{aligned}$$

Our goal is to recover the correct asymptotic limit in the optically thick regime. Using equation (17) with the above modification, we indeed find, assuming for simplicity that the mean free path is uniform, that the numerical flux has the correct asymptotic behaviour given by equation (30):

$$\begin{aligned} \mathbf{F}_{1/2} &\simeq \frac{2\lambda_R}{3\Delta x} \frac{(\mathbf{F}_R + \mathbf{F}_L)}{2} - \frac{\tilde{c}\lambda_R}{3} \frac{(E_R - E_L)}{\Delta x} \\ &\simeq -\frac{\tilde{c}\lambda_R}{3} \frac{(E_R - E_L)}{\Delta x}. \end{aligned} \quad (34)$$

The latter equality comes from the fact that in the limit of optically thick cells, the absorption terms in equation (20) naturally lead to  $F \ll \tilde{c}E$ .

#### 2.4.2 Trapped versus streaming photons

Although the previous method allows us to upgrade, in a straightforward way, our M1 hyperbolic solver for the transport of radiation in a dense, optically thick medium, we have instead implemented in RAMSES-RT an alternative technique, that turns out to be equivalent to the previous one, but allows for a more accurate treatment of the diffusion limit, where trapped photons are advected with the gas, and radiation pressure, along with the work performed by that pressure, is naturally accounted for.

Our technique is based on the ‘IDSA methodology’ (Isotropic Diffusion Source Approximation), proposed by Liebendörfer, Whitehouse & Fischer (2009) in the context of neutrino transport in core collapse SN. The idea is to introduce two different IR photon groups spanning the same frequency range, splitting the total IR radiation energy into a *trapped* radiation energy variable  $E_t$  and a *streaming* radiation energy variable  $E_s$  satisfying  $E = E_t + E_s$ . The difference between the trapped and streaming photons is that the former are assumed to be strictly isotropic in angular space. They correspond to the asymptotic limit of vanishingly small mean free path, for which the radiation flux is strictly zero. We can then rewrite

the radiation moment equations, (20) and (21), using  $\mathbf{F}_t = 0$  as

$$\frac{\partial E_t}{\partial t} + \frac{\partial E_s}{\partial t} + \nabla \cdot \mathbf{F}_s = \kappa_P \rho (caT^4 - \tilde{c}E_t - \tilde{c}E_s) + \dot{E}, \quad (35)$$

$$\frac{\partial \mathbf{F}_s}{\partial t} + \frac{\tilde{c}^2}{3} \nabla E_t + \tilde{c}^2 \nabla \cdot \mathbf{P}_s = -\kappa_R \rho \tilde{c} \mathbf{F}_s, \quad (36)$$

where we used the fact that  $\mathbf{P}_t = E_t \mathbf{1}/3$  (equation 13) since trapped photons are isotropic, and we enclosed the isotropic emission terms from gas, stars, AGN, and other photon groups in equation (21) under one term,  $\dot{E}$ .

Liebendörfer et al. (2009) proposed to split the previous system into two sets of equations, one describing the trapped photons only,

$$\frac{\partial E_t}{\partial t} = \kappa_P \rho (caT^4 - \tilde{c}E_t) + \dot{E}, \quad (37)$$

where the isotropic source of radiation is assigned naturally to the trapped component, and a second one describing the streaming photons only, with

$$\frac{\partial E_s}{\partial t} + \nabla \cdot \mathbf{F}_s = -\kappa_P \rho \tilde{c} E_s, \quad (38)$$

$$\frac{\partial \mathbf{F}_s}{\partial t} + \tilde{c}^2 \nabla \cdot \mathbf{P}_s = -\kappa_R \rho \tilde{c} \mathbf{F}_s - \frac{\tilde{c}^2}{3} \nabla E_t, \quad (39)$$

where the last two equations are our standard moment equations (20) and (21), only with modified source terms. This is the system that we would like to solve using our Godunov scheme. In the Liebendörfer et al. (2009) approach, the next step is to introduce an additional fictitious source term describing the energy exchange between trapped and streaming photons (noted  $\Sigma$  in the IDSA methodology).

We follow a different route, analysing the asymptotic diffusion regime, which gives a straightforward decomposition between trapped and streaming photons. Indeed, in the diffusion limit, we have  $E_s \ll E_t$ , and equation (39) becomes

$$\mathbf{F}_s \simeq -\frac{\tilde{c}\lambda_R}{3} \nabla E_t. \quad (40)$$

On the other hand, we know that the numerical diffusion term for streaming photons in the GLF flux function of our Godunov scheme (equation 17) is

$$\mathbf{F}_s \simeq -\frac{\tilde{c}\Delta x}{2} \nabla E_s. \quad (41)$$

It is then straightforward to make a partition between streaming and trapped photons, such that equation (40) is correctly retrieved in our photon advection scheme. The relations which ensure this are

$$E_t = \frac{3\tau_c}{2} E_s \quad \text{and} \quad E = E_t + E_s, \quad (42)$$

i.e.

$$E_s = \frac{2}{2 + 3\tau_c} E, \quad \mathbf{F}_s = \mathbf{F}, \quad (43)$$

$$E_t = \frac{3\tau_c}{2 + 3\tau_c} E, \quad \mathbf{F}_t = 0. \quad (44)$$

Using this partition, we can describe our streaming photon group with the classical Godunov solver (equation 16) without the additional source term in equation (39), namely

$$\frac{\partial \mathbf{F}_s}{\partial t} + \tilde{c}^2 \nabla \cdot \mathbf{P}_s = -\kappa_R \rho \tilde{c} \mathbf{F}_s, \quad (45)$$

and still get the correct asymptotic diffusion limit of the mixed trapped/streaming system.

In other words, by making the partition of equations (43) and (44) between streaming and trapped photons, in all cells, *before* each photon advection step, the streaming photon variables,  $E_s$  and  $\mathbf{F}_s$ , can be advected using equations (20) and (21), without any modification to the RT advection solver. The RT solver, however, does not touch the trapped photon variable,  $E_t$ . We *de-partition* between the trapped and streaming photons before the thermochemistry step, such that thermochemistry is performed on the total photon density and flux, and *re-partition* once the thermochemistry step is finished, such that the advection is correctly performed in the diffusion limit. The modification to the RHD code to correctly account for the diffusion limit is thus limited to a single new variable ( $E_t$ ), and a few lines of code before and after the call to the thermochemistry.

In addition to this simple modification, we need to also make sure that (i) the trapped photons are advected with the gas, (ii) that radiation pressure from the trapped photons is correctly accounted for, and (iii) that the  $PdV$  work done on the gas by the trapped radiation pressure is accounted for, by reducing the trapped radiation energy accordingly. Fortunately, all these features are automatically acquired in `RAMSES`, by storing the trapped radiation as a non-thermal energy variable. Non-thermal energy variables are a new feature in `RAMSES`, adding up the total energy density and pressure which is used in the classical Euler HD equations (see e.g. R13, equations 39 and 40), and they behave just like the thermal energy. In other words, the trapped radiation energy is correctly advected with the gas, the trapped radiation pressure is correctly accounted for, and so is the  $PdV$  work done by the trapped radiation. These relativistic details are covered in Appendix B. The equation of state relating the trapped radiation energy and pressure, is

$$P_{\text{rad}} = \frac{\tilde{c}}{c} \frac{E_t}{3}. \quad (46)$$

The radiative force is computed as the sum of the trapped and streaming contributions (from equation 36), which, in our model, is also equivalent to the Godunov GLF flux of the streaming photons. The fluid momentum equation (12) thus becomes

$$\frac{\partial \rho \mathbf{v}}{\partial t} + \nabla \cdot (\rho \mathbf{v} \otimes \mathbf{v} + (P + P_{\text{rad}})\mathbf{I}) = \frac{\kappa_{\text{R}} \rho}{c} \mathbf{F}_s + \rho \mathbf{g}, \quad (47)$$

where we omit the contributions from single scattering photon groups, which have the same form as the first term on the RHS. In the diffusion limit, for which  $E_s \ll E_t$  and  $\mathbf{F}_s \approx 0$ , we recover the regime where the radiative force is equal to the radiative pressure gradient

$$\frac{\partial \rho \mathbf{v}}{\partial t} + \nabla \cdot (\rho \mathbf{v} \otimes \mathbf{v} + P\mathbf{I}) = -\frac{\tilde{c}}{3c} \nabla E_t + \rho \mathbf{g}. \quad (48)$$

With the partition given by equations (43) and (44), trapped photons are only generated in regions of the flow where the mean free path is smaller than the cell size. In opposite situations where the mean free path is large enough, it is desirable to make sure that the fraction of trapped photons very quickly converges to zero. We therefore modify our trapped versus streaming photons distribution using

$$E_s = \left[ 1 - \exp\left(-\frac{2}{3\tau_c}\right) \right] E, \quad (49)$$

$$E_t = \exp\left(-\frac{2}{3\tau_c}\right) E. \quad (50)$$

This model has the same optically thick limit as the original one, (equations 43 and 44) but trapped photons vanish much faster in the optically thin limit.

To summarize, our new method starts by initializing the trapped and streaming radiation variables using equations (49) and (50). Only the streaming photons are advected using our original Godunov scheme,

$$\frac{\partial E_s}{\partial t} + \nabla \cdot \mathbf{F}_s = -\kappa_{\text{P}} \rho \tilde{c} E_s, \quad (51)$$

$$\frac{\partial \mathbf{F}_s}{\partial t} + \tilde{c}^2 \nabla \cdot \mathbf{P}_s = -\kappa_{\text{R}} \rho \tilde{c} \mathbf{F}_s. \quad (52)$$

For the thermochemistry, including the radiation/matter coupling term, the IR radiation used is the sum of the free streaming and trapped photons,

$$E = E_t + E_s, \quad \mathbf{F} = \mathbf{F}_s. \quad (53)$$

In our operator splitting approach, the streaming radiation density is in practice advected with equation (51) with the RHS = 0, while the RHSs of equations (37) and (51) are accounted for in the thermochemical coupling of the dust temperature to the *total* IR radiation temperature, as in equations (22) and (23):

$$\frac{\partial}{\partial t} (E_s + E_t) = \kappa_{\text{P}} \rho (caT^4 - \tilde{c}(E_s + E_t)), \quad (54)$$

$$\frac{\partial e}{\partial t} = \kappa_{\text{P}} \rho (\tilde{c}(E_s + E_t) - caT^4). \quad (55)$$

### 3 TESTS

We now describe tests of our RHD implementation, focusing on the new additions. We start with tests of the M1 closure dealing with free streaming and dust-coupled photons, in Section 3.1 and Section 3.2, respectively. Then, in Section 3.3, we analyse the effect of direct radiation pressure from ionizing photons, testing the validity of the momentum transfer from photons to gas. In Sections 3.4–3.6, we go on to test our trapping method for the diffusion of photons in underresolved optically thick regimes. Finally, in Section 3.7 we test the full RHD implementation of multiscattered IR radiation interacting with dust via momentum and temperature exchange, in an occasionally optically thick limit, reproducing the recent 2D experiments of Davis et al. (2014) on the competition between radiation pressure and gravity.

#### 3.1 Free-streaming radiation from a thin disc

In R13, it was demonstrated that while the M1 closure deals well with single sources of radiation, it fails in-between multiple sources, creating spurious sources of perpendicular radiation where opposing radiation flows should more realistically pass through each other. The point of this first test is to investigate how well the M1 method does in a geometry where we might expect it to fail. We are inspired here by a similar test which has been performed by Jiang et al. (in preparation), to compare the behaviour of their variable Eddington tensor (VET; e.g. Jiang et al. 2012) closure against M1 and flux-limited diffusion (FLD).

We consider a multiple source geometry which is quite relevant in the astrophysical context: emission from a thin (galactic) disc, surrounded by a torus of optically thick gas. We compare, in a 2D setup, the converged result of a hydrodynamically static `RAMSES-RT` experiment to an analytically derived result.

The setup is as follows. The simulation box is a square of 1 cm on a side, resolved by  $128^2$  cells. At 0.1 cm from the bottom of the box,

centred along the box width, is an emitting horizontal disc, or line in 2D, since the disc plane is perpendicular to the simulated 2D plane. The disc spans one cell in height, and has a length of  $L = 0.125$  cm, which corresponds to 16 cell widths. For convenience, we define the origin to lie at the centre of the emitting disc, so the disc end coordinates are  $\pm(L/2, 0)$ . The disc has a constant energy density,  $E_0$ , (imposed in every time-step) of monochromatic radiation that only interacts with the gas via hydrogen ionization.

In the background the box contains hot and diffuse ionized gas, while surrounding the disc is a one-cell high torus, in the same plane as the disc, of cold and dense neutral gas which is optically thick to the radiation. The important point is that the background gas is optically thin, allowing the radiation to pass unhindered, while the torus instantly absorbs all radiation that enters it, and re-emits nothing.<sup>6</sup>

For such a setup, the field morphology can be expressed analytically. For any point  $(x, y)$  in the box, a length element  $d\ell$  at location  $(\ell, 0)$  along the emitting disc subtends an angle

$$d\Omega = \frac{y d\ell}{y^2 + (x - \ell)^2}. \quad (56)$$

Assuming isotropic emission and a razor-thin disc, the contribution from  $d\ell$  to the radiation density at  $(x, y)$  is

$$dE(x, y) = \frac{E_0}{2\pi} d\Omega. \quad (57)$$

The energy density at  $(x, y)$  can then be obtained by integrating the contributions from the whole disc:

$$\begin{aligned} E(x, y) &= \int_{\text{disc}} dE(x, y) = \int_{-L/2}^{L/2} \frac{E_0}{2\pi} \frac{y d\ell}{y^2 + (x - \ell)^2} \\ &= \frac{E_0}{2\pi} \left[ \arctan \frac{L/2 - x}{y} + \arctan \frac{L/2 + x}{y} \right]. \end{aligned} \quad (58)$$

In Fig. 1 we map the converged radiation density obtained from RAMSES-RT, in the colour scheme and solid contours, and compare it to equation (58), shown as dashed contours. Comparison of the contours reveals that the M1 scheme does well, though not perfectly, at reproducing the correct result in this astrophysically relevant setup. The discrepancy stems from the well-known disadvantage of the M1 method in dealing with radiation streaming in different directions in the same point, which results in the radiation being too collimated perpendicular to the disc. We stress, however, that *qualitatively*, but not exactly *quantitatively*, the correct morphology is obtained by RAMSES-RT.

### 3.2 Dust absorption

In this test, which is inspired by a similar one from González, Audit & Huynh (2007), we examine how well the M1 method performs in producing the correct radiation morphology in the case of absorption in the optically semithick regime. This is again a pure RT test, with the HD turned off. A 2D square box  $7.48 \times 10^{12}$  cm on a side is resolved with  $64^2$  cells and contains a homogeneous medium with  $\kappa_P \rho = \kappa_R \rho = 10^{-12} \text{ cm}^{-1}$ , making the optical depth of the box  $\tau_{\text{box}} = 7.48$ . The box is illuminated from

<sup>6</sup> For completeness, the properties of the radiation, source, and gas are as follows: the source energy density is  $E_0 = 2.2 \times 10^{19} \text{ erg cm}^{-3}$ , the photon energy is 13.6 eV, and the hydrogen ionization cross-section is  $\sigma_{\text{H}1} = 3 \times 10^{-18} \text{ cm}^2$ . The background gas has density  $10^{-10} \text{ g cm}^{-3}$  and temperature  $10^6 \text{ K}$ , while the torus that surrounds the radiation source has density  $10^{30} \text{ g cm}^{-3}$  and temperature  $100 \text{ K}$ .

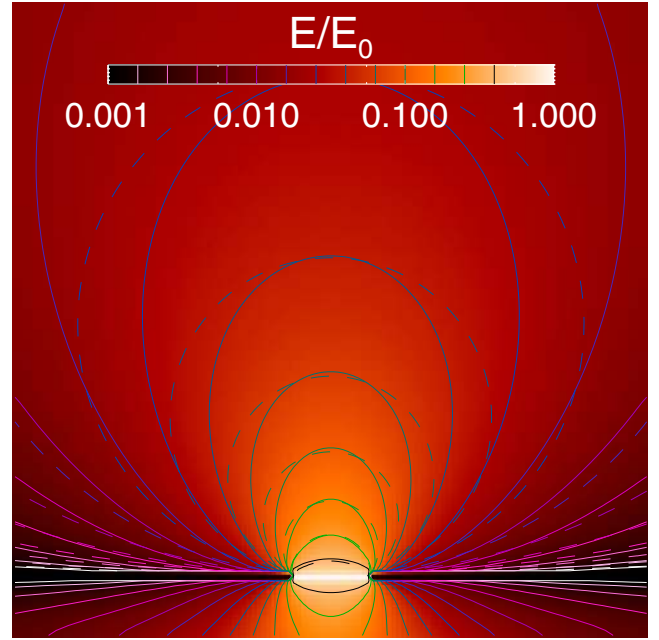


**Figure 1.** Emission from a thin disc. The colour scheme and solid contours show the radiation density obtained by RAMSES-RT, relative to the injected density in the disc at the bottom centre, while the dashed contours show the exact analytic result from equation (58). The contour values are marked in the colour bar. The RAMSES-RT results agree fairly well with the analytic prediction.

the left-hand side by an incoming horizontal flux of radiation  $F_* = 5.44 \times 10^4 \text{ erg s}^{-1} \text{ cm}^{-1}$ . We impose the incoming radiation by setting a constant  $\tilde{c}E = F_x = F_*$ , and  $F_y = 0$  in the left ghost<sup>7</sup> region, and for the remaining three boundaries we set  $E = F_x = F_y = 0$ . We run until a converged static state has been reached (which we verified is independent of the light speed used).

The resulting converged gas temperature profile does not depend on the chosen value for  $\kappa_P$ , as long as it is non-zero to ensure coupling between the radiation and gas temperature, and thus eventual convergence towards  $T = T_r$  (only the time to reach convergence depends on  $\kappa_P$ ). The test is thus equivalent to a pure *scattering* test. We exploit this by comparing the RAMSES-RT results to an equivalent setup run with a computation routine, described in Appendix C, that solves the full RT equation (1) on a four-dimensional grid – with  $64^2$  physical dimensions, and  $32^2$  angular bins. We emit radiation at the rate  $F_*$  in the  $x$ -direction into the left-hand side of the box, and otherwise set zero-valued boundaries for the radiation. The full RT routine does not evolve (or store) the gas temperature, but is run instead in pure scattering mode, with the scattering opacity equal to  $\kappa_R$ . We compare the RAMSES-RT gas temperature to the radiation temperature produced by the full RT routine, which should ideally converge to the same values.

The results are shown in Fig. 2, where we map with colour and solid contours the gas temperature in RAMSES-RT. For comparison, we plot in dashed contours the converged radiation temperature in the full RT calculation. The results agree well in terms of the shape of the radiation field, and the accuracy of the RAMSES-RT produced radiation field is at the  $\sim 10$  per cent level compared to the full RT calculation.

<sup>7</sup> Ghost cells lie exterior to the box boundary on all sides, and define the box boundary conditions. They are necessary for the advection in and out of cells interior to the box boundaries.



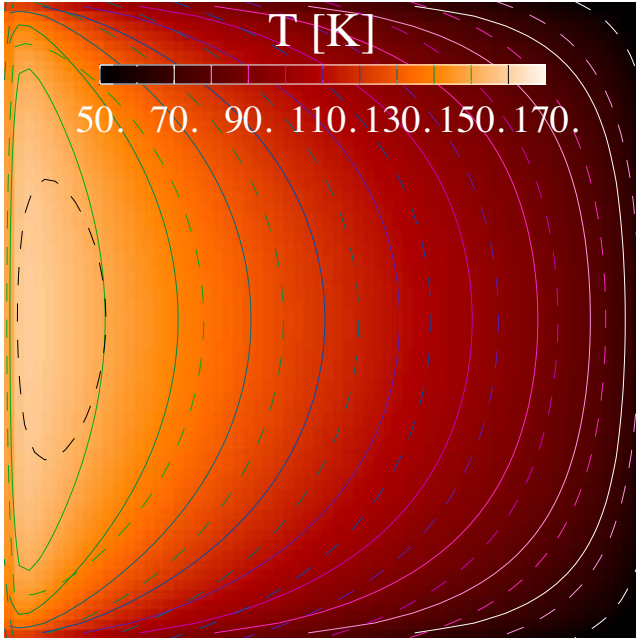


**Figure 2.** Two-dimensional photon scattering test, with an optical depth from side to side of  $\tau_{\text{box}} = 7.48$ . The image shows the equilibrium state reached in the test. The colours and overlaid solid contours indicate the RAMSES-RT gas temperature. For comparison, the dashed contours show results, in the form of *radiation* temperature, from an identical test run with a full RT code. The results produced by RAMSES-RT are qualitatively similar to the full RT results, but differ in value by 10–20 per cent.

The discrepancy can be attributed in part to the M1 moment method directly and its approximative approach to the collisionless nature of radiation, but in part the boundary conditions are to blame, which are not exactly equivalent in RAMSES-RT on one hand and in the full RT code on the other. The zero-valued boundary conditions in M1 ‘suck’ radiation out from the top, bottom, and right-hand sides, while the inwards flux at the right boundary (where the discrepancy is worst) prevents scattered radiation from flowing back out of the box.

### 3.3 Tests of direct pressure from ionizing radiation

We aim to demonstrate with the following RHD tests that radiation pressure in RAMSES-RT is robustly implemented, i.e. momentum is correctly deposited from photons to gas. In what follows, we assume an idealized case of pure hydrogen gas, which is initially homogeneous and isothermal, and monochromatic photons, and we ignore the effect of gravity. The setup is a radiation source of luminosity  $L$  placed at the origin in a medium of homogeneous density  $\rho_0$  which turns on at time  $t = 0$ , and we are interested in following the expansion of the gas due to the direct ionizing radiation pressure. For the tests to be meaningful, we first need analytic expressions to compare against.

#### 3.3.1 Analytic expectations

Wise et al. (2012) present a simple analytic argument to demonstrate the effect of radiation pressure in dwarf galaxies. The expression is derived from requiring momentum conservation in the swept-up gas around the radiation source, ignoring gravity and thermal pressure,

and describes the radial position  $r$  of the expanding density front,

$$r(t) = (r_s^4 + 2At^2)^{1/4}, \quad (59)$$

where  $A = 3L/4\pi\rho_0c$ , and  $r_s$  is the Strömgen radius, at which an optically thick shell forms at  $t \approx 0^8$ ,

$$\begin{aligned} r_s &= \left( \frac{3L}{4\pi\alpha_B n_{\text{H},0}^2 \epsilon_\gamma} \right)^{1/3} \\ &= 1.8 \text{ pc} \left( \frac{L}{L_\odot} \right)^{1/3} \left( \frac{n_{\text{H}}}{1 \text{ cm}^{-3}} \right)^{-2/3}. \end{aligned} \quad (60)$$

Here,  $\alpha_B$  is the case B recombination rate, which we take to be equal to  $2.5 \times 10^{-13} \text{ cm}^3 \text{ s}^{-1}$ , approximately valid in photoionized hydrogen gas,  $n_{\text{H},0} = \rho_0/m_p$  is the hydrogen number density,  $\epsilon_\gamma$  is the monochromatic photon energy, which we take to be the hydrogen ionization energy of 13.6 eV, and we assume a solar luminosity of  $L_\odot = 3.84 \times 10^{33} \text{ erg s}^{-1}$  (in ionizing photons).

We will present expanding H II region experiments where we compare the front position against equation (59). However, we find *at best*, that the simulated expansion only partially follows the analytic prediction. First, the expansion tends to be dominated by photoionization heating, which is not described by equation (59). Secondly, even if the effect of heating is negligible, the expansion eventually stalls due to thermal gas pressure on the far side, leaving a semistable bubble of diffuse ionized gas surrounded by a denser neutral gas. The final radius of the bubble is dictated by the combined effect of photoionization heating and the direct radiation pressure.

We can consider separately, for radiation pressure and photoheating, roughly how far each of these mechanisms are expected to sweep the gas.

For the radiation pressure, ignoring the effect of photoheating, the bubble will reach a radius  $r_\gamma$  where the gas pressure outside the bubble equals the outwards radiation pressure at the surface, i.e.

$$n_{\text{H},0} k_B T_0 = \frac{L}{4\pi r_\gamma^2 c}, \quad (61)$$

where  $T_0$  is the outer gas temperature and  $k_B$  is the Boltzmann constant. Solving for the bubble radius gives

$$\begin{aligned} r_\gamma &= \sqrt{\frac{L}{4\pi c n_{\text{H},0} k_B T_0}} \\ &= 0.28 \text{ pc} \left( \frac{L}{L_\odot} \right)^{1/2} \left( \frac{n_{\text{H}}}{1 \text{ cm}^{-3}} \right)^{-1/2} \left( \frac{T_0}{10^2 \text{ K}} \right)^{-1/2}. \end{aligned} \quad (62)$$

With photoionization heating dominating, the underdense bubble is supported by inner gas pressure, i.e.

$$n_{\text{H},\text{ion}} T_{\text{ion}} = n_{\text{H},0} T_0, \quad (63)$$

where  $n_{\text{H},\text{ion}}$  and  $T_{\text{ion}}$  are the gas density and temperature inside the bubble, somewhat incorrectly assumed to be homogeneous, and the density and temperature outside are just the initial homogeneous values. Given a radius  $r_T$  of the thermally supported bubble, the ionizing luminosity of the central source supports an equal rate of

<sup>8</sup> The creation time of the Strömgen sphere, which is approximately the recombination time, is assumed to be short compared to the hydrodynamical response of the gas, an assumption which holds in our tests (see Fig. 5, though it barely holds in the highest density case).

recombinations in the bubble, i.e.

$$\frac{L}{\epsilon_\gamma} = \frac{4}{3} \pi r_T^3 \alpha_B n_{\text{H,ion}}^2. \quad (64)$$

From this we can solve for the gas density inside the bubble, which we insert into equation (63), giving

$$\begin{aligned} r_T &= \left( \frac{T_{\text{ion}}}{T_0} \right)^{2/3} r_S \\ &= 39 \text{ pc} \left( \frac{L}{L_\odot} \right)^{1/3} \left( \frac{n_{\text{H}}}{1 \text{ cm}^{-3}} \right)^{-2/3} \\ &\quad \times \left( \frac{T_{\text{ion}}}{10^4 \text{ K}} \right)^{2/3} \left( \frac{T_0}{10^2 \text{ K}} \right)^{-2/3}. \end{aligned} \quad (65)$$

We can now compare the radius of the radiation pressure supported bubble versus the radius of the thermally supported bubble. The condition for radiation pressure to start dominating over photoionization heating is

$$r_\gamma > r_T. \quad (66)$$

Substituting equations (60), (62), and (65) then gives the condition

$$\begin{aligned} L &> \frac{1}{n_{\text{H},0}} \frac{T_{\text{ion}}^4}{T_0} \frac{36\pi c^3 k_B^3}{\alpha_B^2 \epsilon_\gamma^2} \\ &= 7 \times 10^{12} L_\odot \left( \frac{n_{\text{H},0}}{1 \text{ cm}^{-3}} \right)^{-1} \left( \frac{T_0}{10^2 \text{ K}} \right)^{-1} \\ &\quad \times \left( \frac{T_{\text{ion}}}{10^4 \text{ K}} \right)^4 \left( \frac{\epsilon_\gamma}{13.6 \text{ eV}} \right)^{-2}. \end{aligned} \quad (67)$$

Admittedly, a range of assumptions and approximations go in, but equation (67) nevertheless gives an idea of the luminosities required for ionizing radiation pressure to give a strong boost over the effect of photoionization heating. Clearly *both* large luminosities and gas densities are required for this to happen. However, the relative difference in the equilibrium radii scales only very weakly with the density and luminosity, i.e.

$$\frac{r_\gamma}{r_T} \propto (L n_{\text{H},0})^{1/6}, \quad (68)$$

so even if the condition of equation (67) is far from met, radiation pressure may well give a modest boost to the thermally driven expansion. Conversely, this also means that a prodigious luminosity and/or density is required for the photoionization heating to become negligible, as is generally acknowledged in the literature (see Krumholz & Matzner 2009, and references therein).

We can also consider the relevant physical scales for ionizing radiation pressure by requiring that it is stronger than the thermal pressure in a Strömgen sphere,

$$\frac{L}{4\pi c r_S^2} > n_{\text{H},0} k_B T_{\text{ion}}. \quad (69)$$

Solving directly for the luminosity gives equation (67) with the outer temperature,  $T_0$ , removed. But for the physical scale, we can instead use equation (60) to eliminate  $n_{\text{H},0}$ , giving the requirement on the Strömgen radius that

$$\begin{aligned} r_S &< \frac{\alpha_B}{12\pi c^2 k_B^2} \frac{L \epsilon_\gamma}{T_{\text{ion}}^2} \\ &= 0.1 \text{ pc} \left( \frac{L}{10^6 L_\odot} \right) \left( \frac{\epsilon_\gamma}{13.6 \text{ eV}} \right) \left( \frac{10^4 \text{ K}}{T_{\text{ion}}} \right)^2. \end{aligned} \quad (70)$$

**Table 1.** Expanding H II region tests. All tests are run in a square box with  $128^3$  cells, with a source luminosity of  $10^6 L_\odot$ , a monochromatic photon energy of 15 eV, and a reduced speed of light factor  $f_c = 10^{-3}$ . The columns list, from left to right, the initial homogeneous gas number density,  $n_{\text{H},0}$ , the expected thermally supported bubble radius,  $r_T$ , direct radiation pressure supported bubble radius,  $r_\gamma$ , the box width,  $L_{\text{box}}$ , the run time of each test,  $t_f$ , and, for comparison, the recombination time  $t_{\text{rec}} = (n_{\text{H},0} \alpha_B)^{-1}$ , which is approximately the time it takes for the Strömgen sphere to develop.

$n_{\text{H},0}$ ( $\text{cm}^{-3}$ )	$r_T$ (pc)	$r_\gamma$ (pc)	$L_{\text{box}}$ (pc)	$t_f$ (Myr)	$t_{\text{rec}}$ (Myr)
$10^0$	291	36	450	$10^3$	$10^{-1}$
$10^3$	2.9	1.1	5.5	10	$10^{-5}$
$10^5$	0.13	0.11	0.3	0.3	$10^{-6}$
$10^7$	$6 \times 10^{-3}$	$11 \times 10^{-3}$	$2 \times 10^{-2}$	$10^{-2}$	$10^{-8}$
$10^9$	$2 \times 10^{-4}$	$11 \times 10^{-4}$	$1.4 \times 10^{-3}$	$10^{-3}$	$10^{-10}$

Comparing with equation (60), this translates to a young stellar population of  $\approx 10^3 M_\odot$  ( $L \approx 10^6 L_\odot$ ), embedded in gas with  $n_{\text{H},0} \sim 10^5 \text{ cm}^{-3}$ , which is currently beyond, but not far from, the resolution limits of most galaxy-scale simulations.

### 3.3.2 Expanding H II regions

We set up a square 3D box and place in the corner a source of luminosity  $L = 10^6 L_\odot$ , emitting monochromatic ionizing photons with energy  $\epsilon_\gamma = 15 \text{ eV}$  ( $1.8 \times 10^{50} \text{ photons s}^{-1}$ ) and hydrogen ionization cross-section  $\sigma_{\text{H I}} = 3 \times 10^{-18} \text{ cm}^2$ , into an initially homogeneous neutral pure hydrogen gas (no helium, metals, or dust) at a temperature of  $10^4 \text{ K}$ . The box boundaries adjacent to the source are reflective and the opposite sides have outflow boundaries. We use  $128^3$  cells, and reduce the speed of light by a factor  $f_c = 10^{-3}$ . Even at this low light speed the run-time is hundreds of light-crossing times in each run, so this has no effect on the later stages of development.

To compare regimes where either ionization heating or ionization pressure dominates, we compare sets of runs at five different initial densities  $n_{\text{H},0}$ , presented in Table 1. For each initial density we run two tests: with and without direct radiation pressure. The table also shows the run time ( $t_f$ ), the box width ( $L_{\text{box}}$ ), and our estimates for the thermally supported bubble radius ( $r_T$ , equation 65) and the direct radiation pressure supported radius ( $r_\gamma$ , equation 62), where we have used a bubble temperature of  $T_{\text{ion}} = 1.3 \times 10^4 \text{ K}$  and an external temperature of  $T_0 = 6 \times 10^3 \text{ K}$ , based approximately on the temperature profiles in the end results (see Fig. 4: the radiation heats the ionized gas, and the shielded neutral gas eventually cools due to residual collisional ionization). Comparing the  $r_T$  and  $r_\gamma$  values in the table, photoionization heating should dominate in the test with the lowest initial density,  $n_{\text{H},0} = 1 \text{ cm}^{-3}$ , but with higher densities radiation pressure should have an increasing effect, and should dominate at the highest initial density of  $n_{\text{H},0} = 10^9 \text{ cm}^{-3}$ .

Fig. 3 shows slices, at the side of the box containing the radiation source, of gas density at the end of each run. Comparing the maps with and without direct radiation pressure, i.e. the upper versus lower row of maps, it is clear that radiation pressure has a negligible

<sup>9</sup> Average ionizing photon energies from young stellar populations are larger by a few eV. However, we use a low photon energy to minimize photoionization heating and give radiation pressure a head start, as higher photon energies increase the heating rate in the H II region.

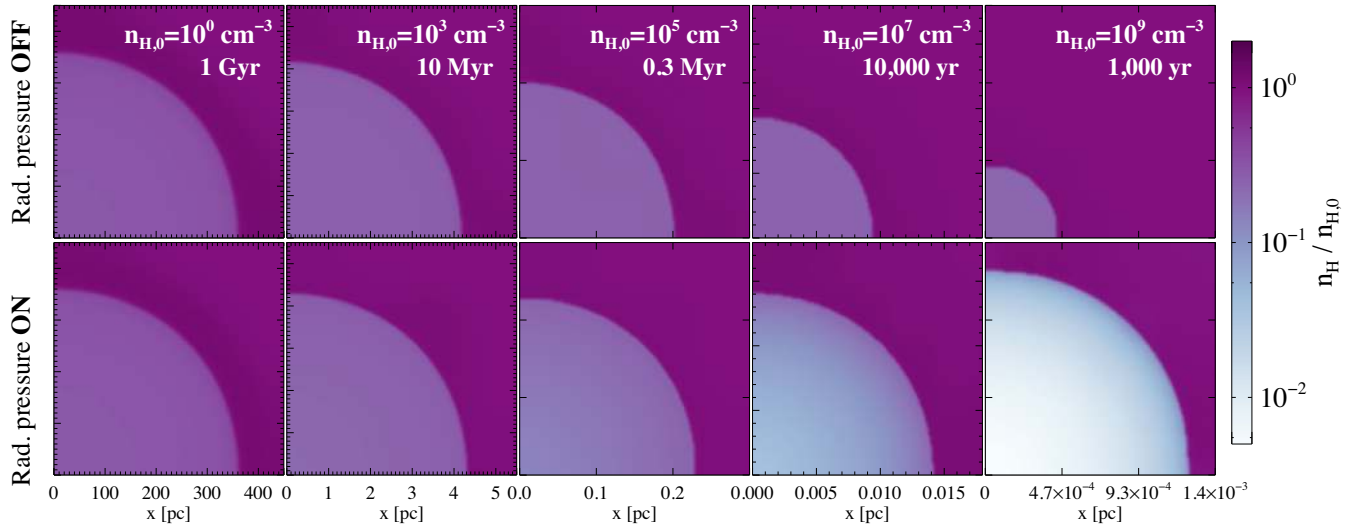


**Figure 3.** Slices of the simulation box, on the side containing the radiation source, showing gas density, normalized to the initial density, at the end of the expanding H II region tests. The upper row shows tests with direct ionizing radiation pressure turned off, i.e. photoionization heating only, and the lower row shows the corresponding runs with the radiation pressure turned on. The panels are ordered from left to right by the initial homogeneous gas density, as indicated in the top-right corner of the upper row panels.

effect at the lowest initial densities, while it gradually overtakes the effect of photoionization heating at higher gas densities. It can also be seen that radiation pressure, once it becomes effective, is more efficient at driving the gas out of the bubble, creating much lower internal densities than with photoionization heating only.

Fig. 4 shows radial profiles of, from top to bottom, gas density, neutral fraction, temperature, and thermal pressure, taking average values in radial bins from the source. We show profiles for two sets of initial densities, one at which radiation pressure is just starting to have an effect ( $n_{\text{H},0} = 10^3 \text{ cm}^{-3}$ , left-hand panel), and the highest initial density, at which radiation pressure clearly dominates ( $n_{\text{H},0} = 10^9 \text{ cm}^{-3}$ , right-hand panel). The density profile plots (top) show how shells of overdense gas are ejected from the ionization-front, leaving behind a semistable bubble of diffuse gas. For the lower-density case (left-hand panels), the profiles with/without radiation pressure are quite similar. The addition of radiation pressure only slightly advances the bubble and yields a slightly lower density and gas pressure at the bubble centre. We note that a similar comparison of profiles at the lowest initial density,  $n_{\text{H},0} = 1 \text{ cm}^{-3}$ , reveals negligible differences between the runs with radiation pressure on or off (not shown), so we are indeed considering densities where radiation pressure is just beginning to have a non-negligible effect compared to photoionization heating.

For the high-density case (right-hand panels in Fig. 4), turning on the radiation pressure has a very substantial effect. Compared to the photoionization heating only case, both the inner bubble density and pressure are almost two orders of magnitude lower, while the temperature remains nearly unchanged. The bubble is now mostly supported by direct radiation pressure, as can be clearly seen by comparing the thermal pressure profiles (bottom-left plot). With only photoionization heating the bubble is supported by thermal pressure, which is identical inside and outside the bubble. With radiation pressure turned on, the thermal pressure drops dramatically inside the bubble and the direct radiation pressure compensates to maintain the large steady bubble, such that the *sum* of gas and radiation pressure is identical on each side of the interface.

Finally, Fig. 5 shows the expansion of the ionization front (I-front, which we define to be at  $x_{\text{H I}} = 0.5$ ), which here is a proxy

for the radius of the underdense bubble, in each of the runs, with the plots ordered by increasing density from top to bottom. We show the I-front expansion as predicted by analytic momentum conservation (equation 59, dashed black), and from the runs, with photoionization heating only (dotted red) and with added direct radiation pressure (solid blue). Grey lines show our estimate of the radiation pressure supported radius  $r_\gamma$  (equation 62, dotted), and the thermally supported radius  $r_T$  (equation 65, dashed), given in Table 1. If the numerical I-front expansion is regarded closely, it can be seen that the front overshoots slightly in all runs, due to the momentum of the expanding gas, and then backtracks to reach a radius where the inner and outer pressure is in equilibrium. This effect can also be seen in the right-hand panel of Fig. 4, if the curves for  $3 \times 10^2$  and  $10^3$  yr are compared.

Two important points can be inferred from Fig. 5. First, the numerical experiments roughly reproduce the analytic expectations, laid out in Section 3.3.1, for the relative roles of photoionization heating and direct radiation pressure. For the lowest initial density (top plot), the bubble radius  $\approx r_T$ , while at the highest density (bottom plot) it goes out to  $\approx r_\gamma$ . The second point is that when radiation pressure dominates the bubble expansion, *and while the bubble is expanding towards its final radius*, the momentum conserving prediction, equation (59), is reproduced by the numerical results (bottom plot).<sup>10</sup>

All in all, these results strongly indicate that RAMSES-RT correctly models direct radiation pressure *and* photoionization heating. As a further validation, the results are qualitatively in good agreement with the numerical experiments of Sales et al. (2014), where ionizing radiation pressure begins to dominate over photoionization heating at similar luminosities and densities as in our case (see their fig. 6).

<sup>10</sup> The analytic result is not reproduced at the very start, at  $t \lesssim 0.001 t_f$ . This is the I-front expansion towards the Strömgen radius, ignored in the arguments leading to equation (59), and during which the gas density stays more or less constant.

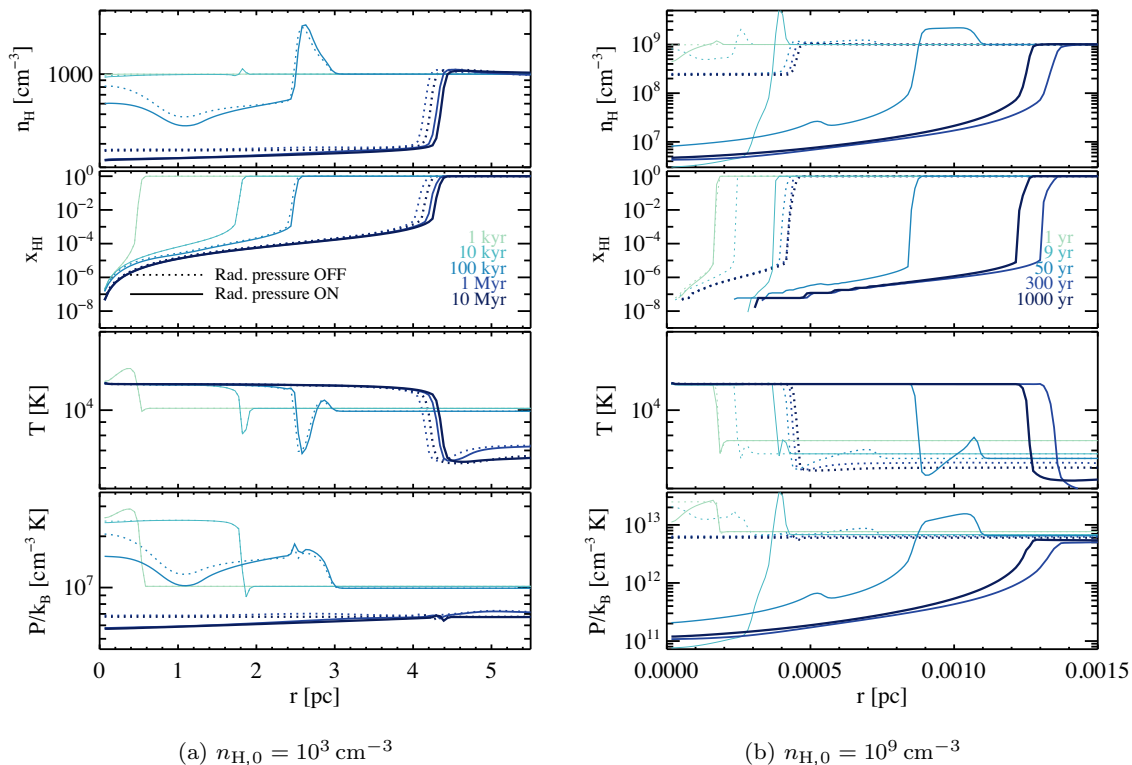


**Figure 4.** Radial profiles of, from top to bottom, the gas density, neutral fraction, temperature, and gas pressure, for the expanding H II region tests, with a  $10^6 L_{\odot}$  source radiating ionizing photons into an initially homogeneous neutral medium. The plots to the left show the case with  $n_{\text{H},0} = 10^3 \text{ cm}^{-3}$ , where radiation pressure has only a marginal effect compared with photoionization heating, and the plots to the right show  $n_{\text{H},0} = 10^9 \text{ cm}^{-3}$ , where radiation pressure dominates over photoionization heating. Runs with only photoionization heating are represented by dotted curves, while runs that in addition include direct pressure from the ionizing photons are represented by solid curves. The curve colours (and thickness) represent the profile times, as indicated in the ionization fraction plots.

### 3.4 Resolved versus unresolved photon diffusion

We will show quantitative tests of photon trapping in the next subsections, but we shall start with a simple demonstration of how it produces robust results when the mean free path is unresolved.

We consider a simple 2D pure RT test, i.e. with the HD turned off. The box contains a homogeneous medium which is optically thick to IR radiation, with an optical depth of  $\tau_{\text{box}} = 200$ . Through the left boundary we emit a constant IR flux of  $5.44 \times 10^4 \text{ erg s}^{-1} \text{ cm}^{-1}$ . The remaining sides of the box have zero-value boundaries. We use a full light speed, but note that the results are independent of the light speed used.

We use this setup in four RAMSES-RT experiments, each running until a steady-state is reached. We run with a low resolution of  $32^2$  cells and a high resolution of  $1024^2$  cells, such that the mean free path is 0.16 and 5.12 cell widths, respectively. For each resolution, we run with and without photon trapping activated.

Without trapping, we should expect more or less correct results in the high-resolution run, where the mean free path is well resolved, but incorrect results in the low-resolution run, where the photons diffuse artificially between the optically thick cells. With trapping turned on, photon diffusion is also handled on unresolved scales, and there should ideally be no difference between the high- and low-resolution runs (on scales larger than the low-resolution cell width). The low-resolution results with trapping should resemble those of the high-resolution run without (and with) trapping.

This is indeed the case, as shown in Fig. 6, where we map the steady-state radiation temperature,  $T_r = (E/a)^{1/4}$ , in the four runs.

Comparing the low- and high-resolution runs without trapping (top-left and bottom-left, respectively), we see a large qualitative difference in the steady-state radiation field. With the unresolved mean free path, the photons diffuse numerically from the optically thick cells, and there is much less build-up of radiation compared to the higher resolution case, where numerical diffusion is negligible. Comparing instead the two runs with trapping turned on (top- and bottom-right), we find similar results, even if the cell widths differ by more than an order of magnitude. Furthermore, the results with photon trapping are also similar to the high-resolution case without trapping, indicating strongly that the photon trapping method (i) reproduces the correct results when the mean free path is unresolved, and (ii) converges to the correct result when the mean free path becomes well resolved.

The agreement is not perfect, as can be seen from a careful comparison of the contours and the box edges. This disagreement stems partly from the fact that the non-trapping result is still not quite resolution converged, but more importantly, with trapping turned on, the box boundary does not behave in the same way along optically thin cells as it does along optically thick ones. In the optically thin limit (lower right), the photons freely escape along the boundaries on scales shorter than the mean free path, and accurately so, since the boundaries are zero-valued. However, when the mean free path is not resolved (upper right), the escape of photons along the boundary is suppressed by the trapping, which essentially assumes the same mean free path everywhere within the cell, resulting in larger values for the radiation temperature.



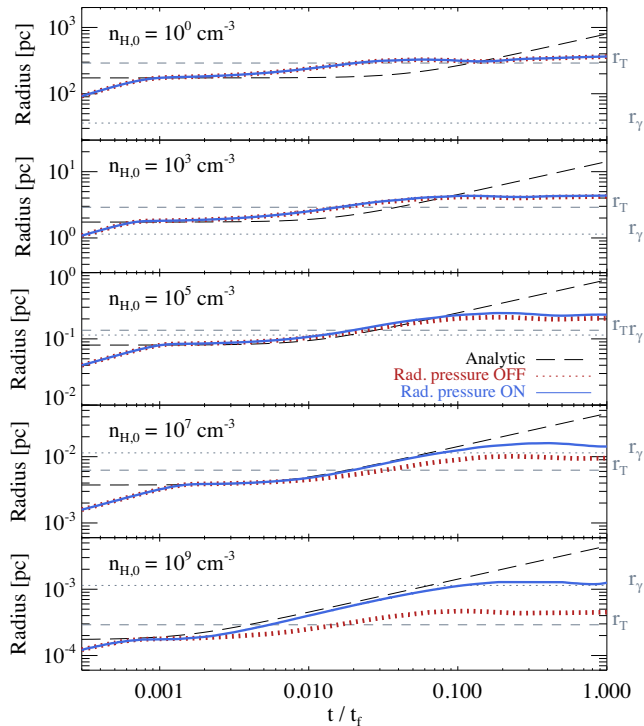


**Figure 5.** Evolution of radiation-powered H II region radius (the radius at which the ionized fraction is 0.5), for increasing initial gas density (top to bottom plot). In each plot, the solid blue (dotted red) curve shows the bubble radius with direct radiation pressure turned on (off), and the black dashed curve shows the analytic expectation from momentum conservation (equation 59). Dashed grey horizontal lines show the expected thermally supported bubble radius ( $r_T$ , equation 65), while dotted grey horizontal lines show the expected radiation pressure supported radius ( $r_\gamma$ , equation 62), where we have used a bubble temperature of  $T_{\text{ion}} = 1.3 \times 10^4$  K and an external temperature of  $T_0 = 6 \times 10^3$  K, based approximately on the temperature profiles in the end results (see Fig. 4). As those simple analytic estimates predict, photoionization heating dominates at the lower densities, but radiation pressure starts to take over at high densities, with an expansion towards the final bubble radius that is well described by momentum conservation. The early deviations from the analytic results, at  $t \lesssim 0.001 t_f$ , correspond to the ionization front expansion towards the Strömgen radius, which in the analytic arguments was assumed to happen instantaneously.

### 3.5 Diffusion of a radiation flash in 2D

We now test whether our implementation of radiation trapping agrees with analytic expectations of diffusing radiation. We consider two test cases, in this and the next subsection. In both cases, HD is turned off.

The first test is a 2D version of the 1D test described in Commerçon et al. (2011). The simulation box is a 1-cm wide square composed of  $128^2$  gas cells, which contain a homogeneous medium with  $\kappa_R \rho = 10^3 \text{ cm}^{-1}$  (i.e.  $\tau_{\text{box}} = 10^3$ ). The box is initially empty of radiation, except for  $\mathcal{N}_0 = 10^5$  photons that are distributed uniformly over four cells at the centre of the box, at which we define the origin of our coordinate system. We then turn on the RT, allowing the photons to diffuse out of the box. For the boundary conditions, we apply linear extrapolation to all the RT variables, from a buffer of two cells inside the border, to determine the values in ghost cells outside the border. We run this test with the full light speed, i.e. with  $\tilde{c} = c$ .

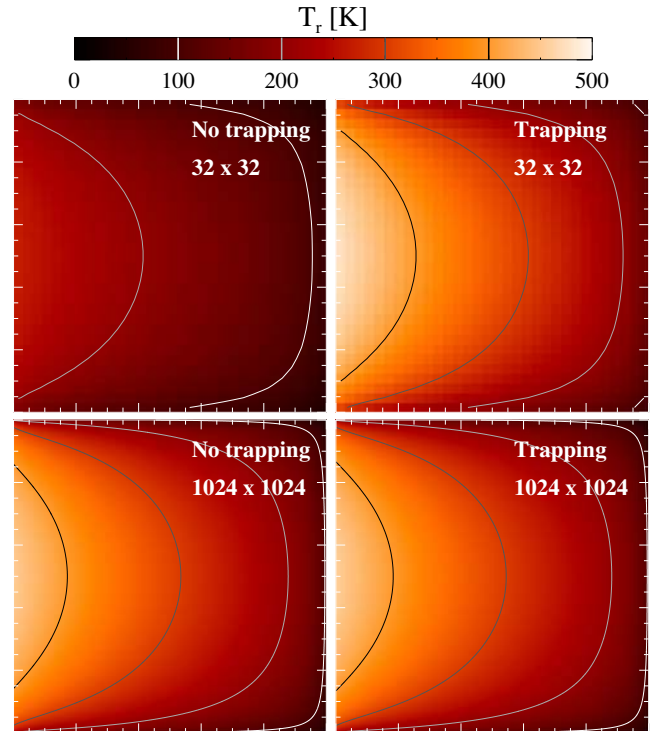


**Figure 6.** A demonstration that our method for photon trapping produces robust results in an optically thick medium, with  $\tau_{\text{box}} = 200$ . All maps show time-converged results from 2D RAMSES-RT runs, with a constant flux of photons into the box from the left. The colour represents the radiation temperature,  $T_r$ , as indicated by the colour bar, and contours mark centennial values, also marked in the colour bar. The top-left map shows the results without photon trapping in a low-resolution run,  $32^2$  cells. The bottom-left map shows an identical run, i.e. no trapping, with a much higher resolution of  $1024^2$  cells. The results are different, since the mean free path is resolved by  $\approx 5$  cell widths in the high-resolution run, whereas a cell width contains  $\approx 6$  mean free paths in the low-resolution run. In the right-hand column of maps we show the results of running with the same pair of resolutions, but with photon trapping activated. With photon trapping on, the results are much better converged with resolution.

The evolution, with time  $t$  and radius  $r$  from the origin, of the photon number density  $N$ , is given by (Commerçon et al. 2011)

$$N(r, t) = \frac{\mathcal{N}_0}{2^p (\pi \chi t)^{p/2}} e^{-\frac{r^2}{4\chi t}}, \quad (71)$$

where  $\chi = c/(3\kappa_R \rho)$ , and  $p = 2$  is the number of dimensions. Fig. 7 shows the time-evolution of the analytic radiation density profile (solid curves), and compares it to the test results (dashed), up to  $5.5 \times 10^{-9}$  s, which corresponds to 165 box crossing times in the free-streaming limit. The numerical results show the sum of the trapped and free-streaming photons (see equation 42). The agreement is excellent. The main discrepancy, at the box edges at late times is caused by the boundary conditions, which release the photons too efficiently.

We note that we also ran the test with a reduced light speed  $\tilde{c} = c \times f_c = c/100$ , reproducing exactly the former results, if the replacement  $c \rightarrow \tilde{c}$  is made in equation (71), and the profiles are plotted at the times  $t/f_c$ , where  $t$  is the profile times in Fig. 7. In other words, reducing the speed of light simply slows the diffusion speed by a factor  $f_c$ .

We also ran the test with 10 times higher and lower optical depth (via  $\kappa_R$ ). At the higher optical depth, the numerical results come

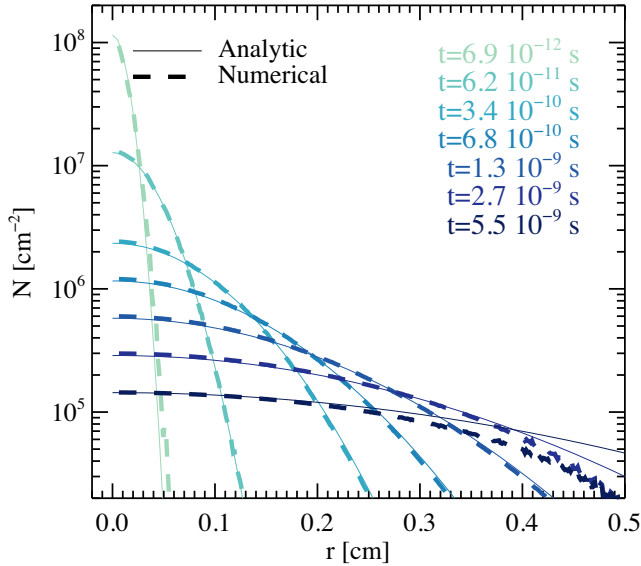


**Figure 7.** Two-dimensional flash diffusion test. Each set of solid (analytic solution) and dashed (numerical solution) curves represents the radial radiation profile at the time given by the line colour, as indicated in the legend. Except near the boundary of the box ( $r = 0.5$  cm), the numerical and analytic results agree well.

even closer to the analytic ones. Conversely, at the lower optical depth, the results visibly diverge from equation (71), as should be expected in the free-streaming radiation limit.

### 3.6 Diffusion of constant luminosity radiation in 3D

We now consider again radiation diffusion with the HD turned off, but in 3D, and with a constant luminosity source. We use a setup, which is relevant for cosmological simulations in terms of the source luminosity, gas density, metallicity, and spatial resolution. We put a source with a luminosity  $L = 10^{50}$  photons  $s^{-1}$  into the centre of a box which is resolved by  $32^3$  cells, and allow the radiation to propagate through the homogeneous gas with the trapping model presented in Section 2.4.2, assuming an opacity  $\kappa_R = 10$   $cm^2 g^{-1}$ , until a converged steady-state has been reached. The box width is  $L_{\text{box}} = 500$  pc, which gives a cell size of 15.6 pc. We then run variants of this setup with varying gas density, spanning  $n_H = 5$ – $10^5$   $cm^{-3}$ , corresponding to optical depths (through the box) of  $\tau_{\text{box}} \approx 0.2$ – $3 \times 10^3$ .

We compare the converged, steady-state, numerical radiation density profile, as a function of distance from the source, to an analytic expression which is derived as follows.

In a homogeneous optically thick medium of density  $\rho$  and emittance  $\mathcal{L}$  (i.e. luminosity per volume), the local photon number density,  $N$ , is described by the diffusion equation,

$$\frac{\partial N}{\partial t} - \frac{\tilde{c}}{3\kappa_R\rho} \nabla^2 N + \mathcal{L} = 0. \quad (72)$$

In the steady-state limit, this reduces to the Poisson equation,

$$\frac{\tilde{c}}{3\kappa_R\rho} \nabla^2 N = \mathcal{L}. \quad (73)$$

In three dimensions, assuming a single point source of radiation, the solution is

$$N(r) = \frac{3\rho\kappa_R L}{4\pi\tilde{c}r}, \quad (74)$$

where  $r$  is the distance to the radiation source, and  $L$  is the point source luminosity. Equation (74) is the analytic expression we can compare to our numerical results.

The analytic argument leading to equation (74) essentially assumes infinity in both space and time, i.e. there are no boundaries or ‘box’ limits, and steady-state can thus only be reached in an infinite time. For time, we simply run the tests until they converge to a final solution, but to approximate the infinite spatial dimensions, we set up the boundaries of the box to roughly match the expected slope given by equation (74).<sup>11</sup> The boundary condition for this test is thus

$$U_0 = U_1 \left(1 - \frac{\Delta x}{L_{\text{box}}}\right), \quad (75)$$

where  $U = (F, N)$  is a cell state,  $\Delta x$  is the cell width at the boundary, and the subscripts 0 and 1 refer to the ghost cell and the boundary cell inside the computational domain, respectively. The boundary can only approximately ‘mimic’ the infinite space assumption, since the box has a square shape.

Fig. 8 shows the results of the diffusion tests, where we have run with a reduced speed of light,  $\tilde{c} = c/200$ . The steady-state limit for radiation flux is the same as with a full light speed, but it takes longer, by a factor  $f_c^{-1}$ , to reach that state. From left to right, the plots in Fig. 8 show the test results for the different gas densities, which translate to different optical depths. In each plot, the grey dash-dotted lines show the  $N \propto r^{-2}$  profile expected for free-streaming radiation, while the solid black lines show the optically thick prediction made by equation (74). The dashed green curves show the converged test results where photon trapping is applied. For comparison, the dotted red curves show the converged results of identical tests where photon trapping is deactivated.

In the optically thick case (leftmost two plots), the radiation profile evolves towards the correct diffusion solution when trapping is included. On close inspection it can be seen that the test results (green dashed) do not perfectly follow the analytic prediction near the edge of the box, but this is purely due to the boundary conditions, which as we remarked are not correct everywhere due to the geometry of the box. If the slope at the boundaries is steepened, the agreement with the analytic result becomes better at  $r \approx 250$  pc, where the edge of the box is closest, but at the same time it becomes worse at  $r \approx 350$  pc, corresponding to the box corners, where the gradient should be shallower.

The third plot from the left shows worse agreement with the analytic solution, but here the gas is also coming close to the optically thin regime, and equation (74) no longer holds. In the rightmost plot we have the situation where  $\tau_{\text{box}} \ll 1$ , and the results agree with the free-streaming limit, regardless of whether trapping is turned on or off.

The curve without trapping assumes the correct  $\propto r^{-1}$  shape where  $\tau_{\text{box}} > 1$  due to the scattering which isotropizes the radiation in every cell, but the curve fails to follow the correct scaling with increasing  $\tau_{\text{box}}$ .

Again we find that our scheme for trapped radiation (Section 2.4.2) robustly reproduces analytic expectations. We ran this test as well with an alternative version of our method for handling the optically thick regime, suggested in Section 2.4.1, where instead

<sup>11</sup> In the tests with the most optically thick gas, free-flow boundary conditions result in an overestimate of the radiation in the box, since the gradient at the box edge is zero, giving too much backflow of radiation from the boundaries, while zero-valued boundaries give an underestimate because the gradient is infinite, and hence no backflow comes from the boundaries.

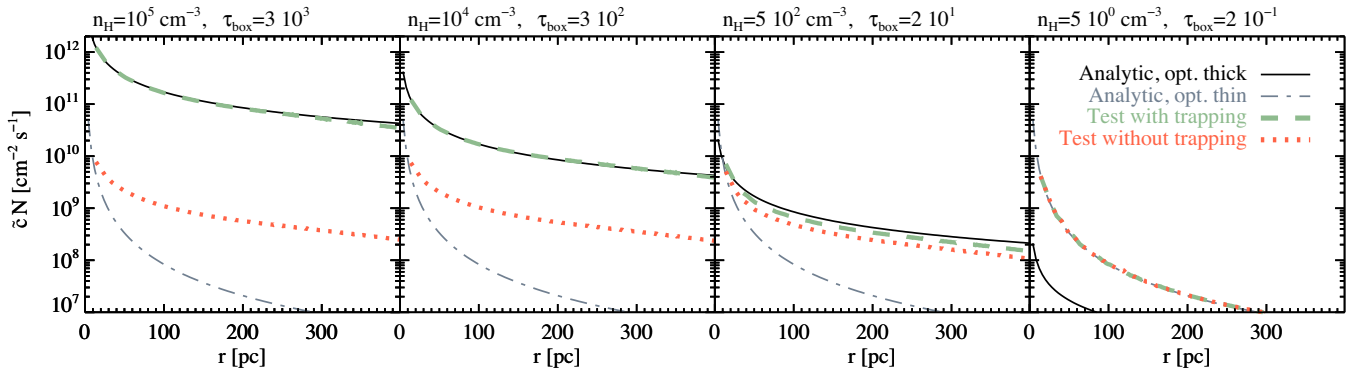


**Figure 8.** Test of radiation diffusion in a medium of decreasing optical thickness (from left to right). The plots show time-converged radiation profiles from the source at the centre of the box in radiation tests with and without trapping (green dashed and red dotted lines, respectively). The solid black lines show the analytic solution to the diffusion equation, equation (74), which the tests with trapping should reproduce in optically thick gas. The grey dot–dashed lines show the analytic solution for free-streaming radiation, which the tests should reproduce for vanishing optical thickness, regardless of whether trapping is turned on or off.

of splitting the photons into trapped and free-streaming, we apply directly a diffusion operator  $\alpha(\tau_c) = (1 + 3/2 \tau_c)^{-1}$ , where  $\tau_c$  is the cell optical depth, to the GLF intercell flux function, as in equation (34). The results using this alternative version were identical to using the trapped/streaming photons scheme, which is no surprise, since the trapped/streaming split essentially amounts to the same thing for the intercell flux. However, the trapped/streaming scheme has the further advantages of the trapped photons moving with the gas, and of a natural inclusion of radiation pressure in the optically thick regime, neither of which is an issue in this test.

### 3.7 Levitation of optically thick gas

As a final test of radiation pressure, the radiation–temperature coupling, multiscattering, and photon trapping, we repeat the 2D experiment described by Krumholz & Thompson (2013) and Davis et al. (2014), hereafter **KT13** and **D14**, respectively, which explores the competition between gravity and radiation pressure.

The experiment is interesting in the context of radiation feedback, because it gives insight into how gravitationally bound gas responds to multiscattering radiation pressure. The setup, which represents a stellar nursery or the central plane of an optically thick galactic disc, consists of a thin bottom layer of gas, kept in place by gravity, which is then exposed to an opposing flux of IR radiation. Even though the radiation flux is sub-Eddington, the effect of multiscattering may still lift the gas if the radiation is efficiently trapped by the gas. However, radiative Rayleigh–Taylor instabilities, if they develop, suppress the radiation pressure by creating ‘chimneys’ through which the radiation may escape without efficiently coupling to the gas.

**KT13** ran the experiment using the FLD method, which essentially solves equation (30), while making sure the radiation does not surpass the speed of light in the optically thin limit. They found that the radiation tends to escape through the gas rather than coherently lifting it, resulting in a ‘steady-state’ of turbulent gas boiling near the radiating bottom surface.

**D14** investigated the idea that the failure to lift the gas has to do with the RT method. This is a valid concern, since the mean free paths are, for the most part, resolved in the experiment, but FLD is strictly only valid in the optically thick regime. They ran the experiment with the *ATHENA* moment method RHD code, comparing

the FLD closure against the more accurate VET closure, which constructs the radiation flux vector on the fly in every volume by sweeping the grid with short characteristics rays, thus incorporating the contribution from all radiation sources and absorbers. They found that the qualitative result is sensitive to the closure used, with their FLD implementation giving a similar result as found by **KT13**, while the VET version coherently lifts the gas out of the frame. However, while the average horizontal velocity of the gas is considerably higher with VET, the average optical depths and radiation force on the gas are quite similar between the two methods: the defining difference appears to be that the radiation force with VET is just enough to lift the gas while with FLD it is just below what is needed. The reason, the authors conclude, is that as the gas is being lifted, the FLD closure tends to create chimneys in the gas through which most of the radiation escapes, and hence the force is enough to get the gas moving and forming those chimneys, but the radiation never builds up sufficiently to evacuate the gas.

The M1 closure can be seen as an intermediate approach between those of FLD and VET: instead of simply following the energy gradient as in FLD, M1 stores locally the bulk direction of radiation, keeping some ‘memory’ of where it was emitted. However, the directionality of radiation from multiple sources tends to mix locally, creating an artificial diffusion which should be more or less absent with the VET closure, provided good angular resolution in the VET ray-sweeping scheme. We should therefore expect our results with M1 to lie somewhere between those of FLD and VET, though a priori it is unclear exactly where. None the less, the quantitative results using the FLD and VET closures in **D14**, in terms of effective optical depths, radiation force, and even gas velocities, lie within a fairly narrow margin, making this a good test case for our implementation. We thus repeat the test from **D14** and validate our implementation by comparing our results to theirs.

The setup of the experiment is as follows: the simulation box is a 2D square of height  $L_{\text{box}} = 1024 h_*$ , where  $h_* = 2 \times 10^{15}$  cm is the scaleheight for the initial gas density profile. The box is resolved by  $2048^2$  cells, and the resolution is fixed, i.e. we do not use adaptive refinement. The physical resolution and box height is identical to that of **D14**, while the box width, constrained by the square geometry of *RAMSES*, is twice as large. A layer of gas is placed at the bottom of the box, and given an exponential density profile with distance from the bottom,  $\rho(h) = \rho_* \exp(-h/h_*)$ ,

where<sup>12</sup>  $\rho_* = 7.1 \times 10^{-16} \text{ g cm}^{-3}$ , resulting in a column density of  $\Sigma = 1.4 \text{ g cm}^{-2}$ . Following D14, we add fluctuations to the initial gas density profile, of the form

$$\frac{\partial \rho}{\rho} = 0.25 (1 \pm \chi) \sin(2\pi x/L_{\text{box}}), \quad (76)$$

where  $\chi$  is a random number in the range  $[-0.25, 0.25]$ . The initial gas profile is floored at a minimum density of  $10^{-10} \rho_*$ , and the gas is given a homogeneous initial temperature of  $T_* = 82 \text{ K}$ . The only non-adiabatic source of heating and cooling for the gas is the dust–radiation interaction,

$$\frac{\partial e}{\partial t} = -\frac{\partial E}{\partial t} = \kappa_{\text{P}} \rho (\tilde{c}E - caT^4). \quad (77)$$

The bottom boundary of the box emits a radiation flux of  $F_* = 1.03 \times 10^4 \text{ erg cm}^{-2} \text{ s}^{-1}$  ( $2.54 \times 10^{13} L_{\odot} \text{ kpc}^{-2}$ ), and the box is initialized to contain an upwards radiation flux of the same magnitude, with  $\tilde{c}E = F_y = F_*$  and  $F_x = 0$ , and thus a radiation temperature

$$T_{\text{r}*} = \left(\frac{F_*}{ca}\right)^{1/4} = T_*. \quad (78)$$

The radiation is coupled to the gas via Rosseland and Planck opacities which, vitally to the mechanics of this experiment, are functions of the gas temperature:

$$\begin{aligned} \kappa_{\text{P}} &= 0.1 \left(\frac{T}{10 \text{ K}}\right)^2 \text{ cm}^2 \text{ g}^{-1}, \\ \kappa_{\text{R}} &= 0.0316 \left(\frac{T}{10 \text{ K}}\right)^2 \text{ cm}^2 \text{ g}^{-1}. \end{aligned} \quad (79)$$

These opacity functions originate from KT13 and are approximately in agreement with dust models at  $T \lesssim 150 \text{ K}$  (Semenov et al. 2003). Given the initial temperature,  $T_* = 82 \text{ K}$ , the initial Rosseland opacity is  $\kappa_{\text{R}*} = 2.13 \text{ cm}^2 \text{ g}^{-1}$ .

The radiation force is countered by a homogeneous gravitational acceleration field pointing downwards, of magnitude  $g = 1.46 \times 10^{-6} \text{ cm s}^{-2}$ . The local competition between downwards gravity and upwards radiation pressure is described by the Eddington ratio,

$$f_{\text{E}} = \frac{f_{y,\text{rad}}}{g\rho}, \quad (80)$$

where  $f_{y,\text{rad}}$  is the vertical radiation force,

$$f_{y,\text{rad}} = \frac{\kappa_{\text{R}} \rho F_y}{c} + \frac{1}{3} \nabla E_{\text{r}}. \quad (81)$$

Given the initial conditions, the Eddington ratio is  $f_{\text{E},*} = 0.5$ , so the radiation initially cannot lift the gas against the opposing force of gravity. However, the gas is optically thick to the radiation with an initial optical depth of, from bottom to top,

$$\tau_* = \kappa_{\text{R}*} \Sigma = 3. \quad (82)$$

Thus, the radiation can be trapped and accumulated by the layer of optically thick gas, which boosts the radiation temperature. Due to the coupling in equation (77), this in turn heats the gas, which may via equation (79) increase  $\kappa_{\text{R}}$  to the extent that  $f_{\text{E}} > 1$ . This of

course requires efficient trapping of the radiation, which is the vital factor that in the end decides whether the gas is lifted or not.

It should be noted that *trapping* here not only refers to our method for trapping radiation in regions where the optical depth is unresolved, but also to radiation which may be free-streaming in optically thin gas, but is trapped bouncing back and forth between the confinements of optically thick shells. We do apply our method of trapping photons *inside* gas cells of unresolved mean free path, which turns out to be relevant only to the early lift of gas, as we shall see in the following analysis.

The box is periodic in the horizontal direction, both for the radiation and matter. For the matter content, the bottom of the box is reflective, allowing no escape or entry of gas, and Dirichlet boundary conditions, i.e. fixed values, are applied to the top, with  $\rho = 10^{-13} \rho_*$ ,  $T = 10^{-3} T_*$ , and zero velocity, in pressure balance with the initial conditions, and allowing easy escape of upwards moving gas. For the radiation, we also apply Dirichlet boundary conditions at the top, with zero flux and energy density. The bottom boundary needs to emit radiation vertically at the rate  $F_*$ . We accomplish this by solving the GLF intercell flux function (equation 16) to give an intercell flux of  $F_{1/2} = F_*$  at the interface between each cell at the lower box boundary and its ghost neighbour, with the additional requirement that the ghost region cell has a photon flux of  $F_0 = (0, F_*)$ . This gives a radiation energy density for the ghost cell of

$$\tilde{c}E_0 = F_* - F_{y,1} + \tilde{c}E_1, \quad (83)$$

where the subscripts 0 and 1 refer to the ghost cell and the boundary cell inside the computational domain, respectively. As with all other tests presented in this paper, we use here the GLF intercell flux function for calculating the photon advection between cells. We tried as well with the HLL intercell flux function, which is better at maintaining the directionality of radiation (see R13), though photon trapping is strictly not supported with it (see comment in Section 2.2). Using HLL results in slightly more efficient early lift of gas than with the GLF function, but eventual convergence towards the same qualitative situation at the end of the run.

We follow the evolution of the system for  $200 t_*$ , where  $t_* = h_*/c_*$  is the characteristic sound crossing time, and  $c_* = \sqrt{k_{\text{B}} T_*/(\mu m_{\text{H}})} = 0.54 \text{ km s}^{-1}$  is the characteristic sound speed. We run the experiment using a reduced light speed of  $\tilde{c} = 3 \times 10^{-3} c$ , which is more than two orders of magnitude faster than  $c_*$  (and much faster than any gas velocities attained in the experiment). We *start* the experiment at a full light speed and converge exponentially towards  $\tilde{c}$  over  $3 \times 10^4$  RHD time-steps. We do this specifically to capture the sudden and short lived pile-up of trapped photons by the gas which is accumulated mostly in the bottom layer of cells. This only affects the acceleration of gas in the initial few  $t_*$ , compared to running at  $\tilde{c}$  for the whole experiment. We have run as well with a factor of 10 lower value for  $\tilde{c}$ , which gives a very similar evolution, implying light speed convergence around the default value. In all the results presented here, we use the relativistic corrections described in the appendix, but note that they have no visible effect on the results.

To illustrate the effect and importance of photon trapping, we present results from two RAMSES-RT runs, one with and one without photon trapping. The run without trapping uses  $\tilde{c}$  for the whole run, without the initial decrement from the full light speed, as this has no effect without the trapping mechanism which is responsible for the initial pile-up of radiation. Also, since the run without trapping has much less initial vertical acceleration of gas, it has half the box width (and height) as the one with trapping activated, while

<sup>12</sup> Since the experiment is in 2D, the units for density and column density should be  $\text{g cm}^{-2}$  and  $\text{g cm}^{-1}$ , respectively. However, following KT13 and D14, we use 3D units in the description for this experiment.



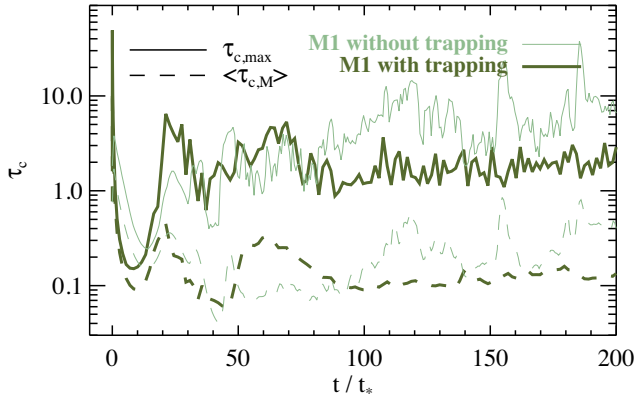


**Figure 9.** Maximum (solid) and mass-weighted average (dashed) cell optical depths in the gas levitation test. The thin bright-green curves show a run without radiation trapping, while the thick dark-green curves show the main run with radiation trapping. The high optical depths of cells indicate that the diffusion limit is somewhat relevant in this experiment, especially at the very start of the runs ( $t \lesssim 5t_*$ ), where most of the gas mass is in the diffusion limit ( $\tau_c \gtrsim 1$ ).

keeping the same physical resolution, i.e. the box has a height of  $L_{\text{box}} = 512 h_*$  and is resolved by  $1024^2$  cells.

Fig. 9 shows the evolution of cell optical depths,  $\tau_c$ . Focusing first on the run without trapping (light green curves), we find that the mass-weighted average and maximum cell optical depths start at  $\langle \tau_{c,M} \rangle \approx 2$  and  $\tau_{c,\text{max}} \approx 4$ , respectively, showing that the mean free paths are unresolved at the start of the run, which implies that the diffusion limit, and thus the photon-trapping mechanism, is relevant at the start. The cell optical depths quickly decline in value as the gas rises from the bottom and becomes more diffuse, such that the mean free path becomes better resolved. For the remainder of the run the average cell optical depths are mostly well below unity, although there always remain cells with large optical depths. With trapping turned on (darker green curves), the optical depths start well above the values from the non-trapping run, due to the larger concentration of photons that now accumulates in the optically thick gas, which leads to higher gas opacity via equation (79). However, once the gas starts to lift, the cell optical depths are reduced to smaller values than in the non-trapping run, as a result of the diffusive pressure of the trapped photons. After the experiment has reached a turbulent equilibrium state, around  $100 t_*$ , the opacities are consistently lower than when trapping is not used.

Fig. 10 shows maps of gas density and radiation temperature at different snapshots of the run with photon trapping. The evolution is qualitatively similar to the results in D14, and we see the same features of filamentary gas concentrations interspersed with more diffuse ‘chimneys’ through which the radiation escapes to the top of the box. Visual inspection of the gas density and radiation temperature suggests that the results fall in between those of FLD and VET in D14 (their figs 3–5). Focusing on the gas densities, the gas is initially levitated quite efficiently, even more so than in either FLD or VET, due to the strong initial trapped photon pressure (a point which we will revisit later). About 1 per cent of the total mass is ejected from the top of the box in the first upwards burst of gas. The rest of the gas drops back to the bottom, to  $\lesssim 200 h_*$ , where it is kept turbulent by the competition between radiation pressure and gravity. Unlike with VET, the gas is not coherently lifted beyond

$h \approx 500 h_*$ .<sup>13</sup> It settles to eventually occupy similar heights as in the FLD results, where it is concentrated below  $\approx 200 h_*$  at  $t = 150 t_*$ . The radiation temperature maps show trapped radiation beneath coherent layers of gas, which extends quite high initially, but is kept at much lower heights once the gas breaks up due to Rayleigh–Taylor instabilities.

The first two density maps from the left ( $t = 25$  and  $50 t_*$ ) contain a conspicuous perfectly vertical feature at  $x \approx 575 h_*$ . This gas is flowing downwards in a thin stream, which is limited in thickness only by the cell width. The horizontal forces on the gas stream are negligible for some time, and thus, guided by the grid alignment, the stream can maintain this perfect shape from  $t \approx 22 t_*$  until it is destroyed by laminar gas flows at  $t = 64 t_*$ . No other such numerical features appear in the simulation.

In Figs 11 and 12 we compare our results directly to those of FLD and VET from D14 (courtesy of Shane Davis). The top plot in Fig. 11 shows the volume-averaged Eddington ratio,

$$f_{E,V} = \frac{\langle f_{y,\text{rad}} \rangle}{\langle g\rho \rangle}. \quad (84)$$

This ratio expresses the competition between radiation pressure and gravity, with  $f_{E,V} > 1$  when radiation pressure has the upper hand. By construction,  $f_{E,V} = f_* = 0.5$  at the start of the run. The middle plot shows the volume-averaged optical depth from bottom to top,

$$\tau_V = L_{\text{box}} \langle \kappa_R \rho \rangle. \quad (85)$$

The evolution of this quantity is closely linked to  $f_{E,V}$  through that of  $\kappa_R$ , which sets both the optical depth and the strength of the radiation pressure. The bottom plot shows the ratio of the photon flux-weighted mean optical depth,

$$\tau_F = L_{\text{box}} \frac{\langle \kappa_R \rho F_y \rangle}{F_y}, \quad (86)$$

to  $\tau_V$ .

We first focus on the effect of photon trapping in the RAMSES-RT runs (Fig. 11, light and dark green curves). With photon trapping turned on, there is an almost instantaneous rise from the initial values,  $f_{E,V} = 0.5$  and  $\tau_V = 3$ , quickly followed by a steep decline in both. This early evolution is absent in the non-trapping run, which just shows a gradual and much slower initial rise for both quantities. The steep rise is due to the sudden build-up of trapped photons in the bottom layer of cells, which increases  $\kappa_R$ . This results in a strong force from the diffusive radiation, which quickly pushes the gas upwards. The rapid diffusion of the gas in turn leads to a rapid decrease of  $\kappa_R$ , and some of the trapped radiation escapes upwards, reducing the opacity and the radiation push. With trapping turned off, there is much less initial build-up of radiation, and the initial push is gentler. In the long run, ignoring the evolution in the first  $\approx 10 t_*$ , the evolution with/without trapping, however, is quite similar.

The same can be said if we compare the RAMSES-RT results to those from D14. The results agree quite well overall, showing similar early reaction and then settling on similar semiconstant values of  $f_{E,V}$ ,  $\tau_V$ , and  $\tau_F/\tau_V$ . In the early reaction phase,  $t \lesssim 75 t_*$ , the results in places resemble an interpolation between the FLD and VET results, in line with our argument that M1 is an intermediate approach between FLD and VET.

<sup>13</sup> The VET simulation is restarted with an extended box height at  $t = 80 t_*$ , when the gas approaches the upper boundary, and the gas is approaching the (new) upper limit at  $h \approx 2048 h_*$  when the run is stopped at  $\approx 150 t_*$ .

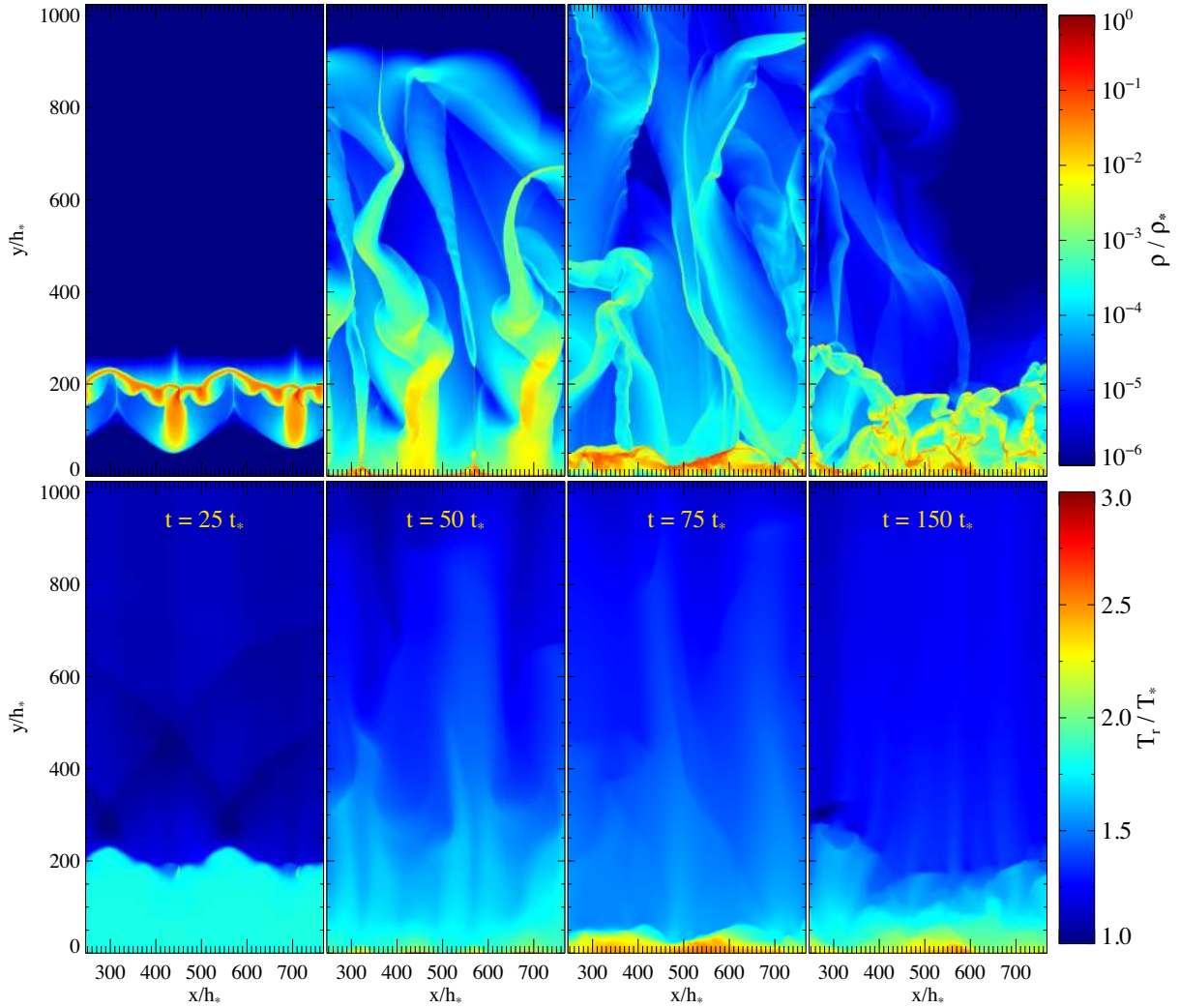


**Figure 10.** Maps of the gas density (upper row) and radiation temperature (lower row) in selected snapshots from the gas levitation experiment. We show the full height of the box, but to fit the maps on the page, we show only half of the width, along the centre.

The run with photon trapping very quickly reaches peaks of  $f_{E,\nu} = 10$  and  $\tau_\nu = 32$  at  $0.023 t_*$ , which disappear rapidly as the gas starts moving. We do not show these peaks in the plots in Fig. 11 for the sake of not stretching out the  $y$ -axes. The magnitude of the peaks depends on the speed of light, which is the reason why we start the trapping run with a full speed of light and converge to  $\tilde{c}$  in the first  $\approx 3 \times 10^4$  time-steps. We verified in hydrodynamically static runs (i.e. with RT turned on but the HD turned off) that an equilibrium is reached with constant values of  $f_{E,\nu} = 10.7$  and  $\tau_\nu = 32.5$ , regardless of the speed of light. The important differing factor is simply the time it takes to reach that equilibrium, which with reduced light speed becomes longer than the duration of the peak.

This rather large discrepancy in optical depth from the FLD and VET implementations at early times demands further investigation to justify our ballpark numerical value. If we assume, for the sake of simplicity, that all the gas is initially placed in a single horizontal cell layer,<sup>14</sup> we can derive an expression for the equilibrium value

<sup>14</sup> This is a good approximation: 25–60 per cent of the column density is initially in the bottom layer of cells, depending on the sinusoidal and random fluctuations.

of the cell optical depth,  $\tau_c$ , at which the upwards flux from the cell equals  $F_*$ . In the framework of M1 using the GLF intercell flux, with photon trapping, such an equilibrium is met when

$$\tilde{c}E_s = \left[ 1 - \exp\left(-\frac{2}{3\tau_c}\right) \right] \tilde{c}E = 2F_*, \quad (87)$$

where  $E_s$  is the  $\tau_c$ -dependent streaming photon density (equation 49). We can then combine the relation  $\tau_c = \kappa_R \Sigma$ , equation (79) describing  $\kappa_R(T)$ , and the relation between radiation temperature and radiation energy, yielding

$$\tau_c(E) = 3.16 \times 10^{-4} \frac{\text{cm}^2 \text{g}^{-1}}{\text{K}^2} \Sigma \sqrt{\frac{\tilde{c}E}{ca}}, \quad (88)$$

assuming  $T_r = T$ . Substituting equation (88) into equation (87), and using  $\Sigma_*$ , then gives an equilibrium condition that can be solved for  $\tau_c$ , which yields a median value of  $\tau_c = 27$ , in fair agreement with our peak optical depth of 32. Allowing for the maximum fluctuation amplitude in  $\Sigma_*$  gives an upper limit of  $\tau_c = 67$ , and looking at Fig. 9, we find that the maximum initial values for  $\tau_c$  are within this limit.

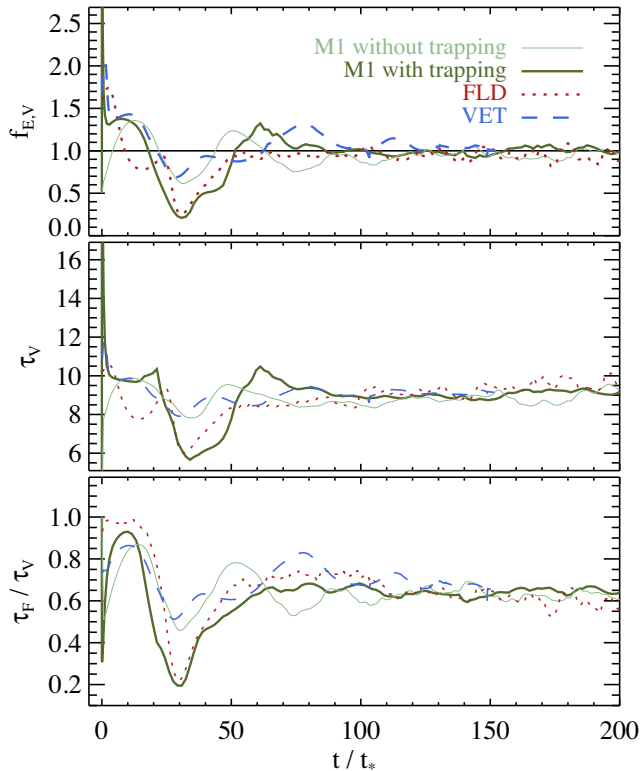


**Figure 11.** Comparison of gas levitation test for RAMSES-RT with and without trapping (light green and darker green curves, respectively), and for the ATHENA code, taken from D14, using FLD (red) and VET (blue). Top panel: Eddington ratio  $f_E (=0.5$  at  $t = 0$ ) between the upwards force of radiation pressure and the downwards force of gravity. Middle panel: average volume-weighted optical depth along lines of sight from the bottom to the top of the box ( $=3$  at  $t = 0$ ). Bottom panel: ratio between the flux-weighted and volume-weighted average optical depths ( $=1$  at  $t = 0$ ). All plots show strong similarity between the different methods and codes. Comparison of the RAMSES-RT results with and without trapping reveals that the diffusion limit is important at the beginning of the run, where a pile-up of radiation results in very strong optical depth and in turn a strong radiation force.

With FLD we can make a similar estimate. Here the equilibrium condition is

$$\frac{\tilde{c}E}{3\tau_c} = F_*, \quad (89)$$

and again using equation (88) gives the same median and upper limit for  $\tau_c$  as in the photon-trapping framework. While these simplified estimates do not predict the exact equilibrium value of the optical depth, they demonstrate that the high initial peak reached in our run is indeed plausible.

We now turn our attention to the gas velocities. The upper panel in Fig. 12 shows the ratio of the mass-weighted mean (i.e. bulk) vertical velocity and the characteristic sound speed, while the lower plot shows velocity dispersions in the gas (i.e. turbulence). Without trapping, the M1 results show relatively weak initial upwards acceleration of the gas, followed by a drop, a bounce, and then a turbulent equilibrium state, with the velocity dispersions well below the constantly rising ones of VET, but somewhat above those of FLD. With trapping turned on, there is a much more dramatic initial acceleration of gas, even stronger than that of VET, which we already attributed to the strong initial build-up of trapped radiation in and below the bottom layer of gas. This is followed by a very strong deceleration and drop back to the bottom of the box, which

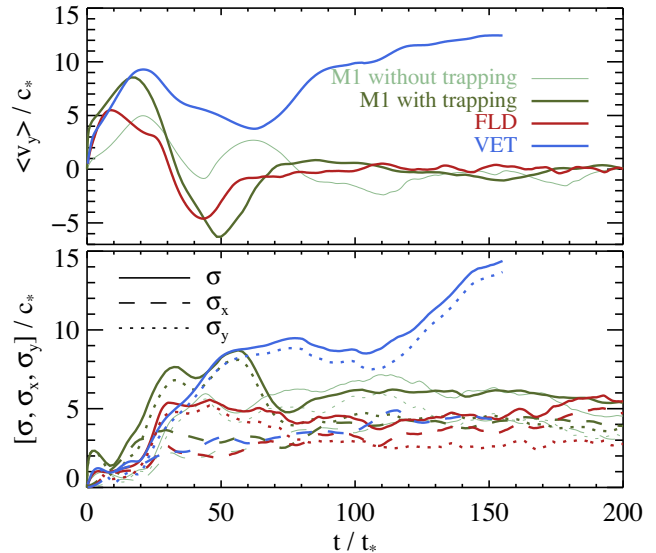


**Figure 12.** Gas velocity comparison in gas levitation test, for RAMSES-RT with and without trapping (light green and darker green curves, respectively), and for the ATHENA code from D14, using FLD (red) and VET (blue). Top plot: mass-weighted mean vertical velocity. Bottom plot: mass-weighted velocity dispersions. The plots show good comparison between RAMSES-RT and ATHENA, but the RAMSES-RT results are more in line with the ones obtained with FLD than VET. The main effect of photon trapping in RAMSES-RT can again be seen in the faster early acceleration due to the combination trapped photon pressure and the higher opacity of the gas that results from the trapped photons (equation 79).

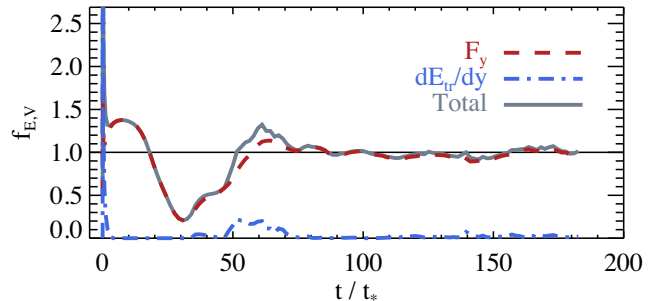


**Figure 13.** Contributions, in the M1 levitation test with trapping, to the total Eddington ratio (grey), from the free-flowing photon flux (red) and the diffusion pressure from trapped photons (blue). The diffusion pressure is important, but only at the very start of the run where almost all the gas mass is concentrated in one row of cells at the bottom of the box.

is even stronger than with FLD. The strong drop is likely due to the reduced speed of light: the incoming radiation flux cannot keep up with filling the growing ‘bubble’ between the bottom of the box and the rising layer of gas, and as a result the radiation pressure deflates as the gas lifts. At the same time, radiative Rayleigh–Taylor instabilities fragment the gas, allowing the radiation to escape, and the gas falls hard back to the bottom. However, it also bounces back, and eventually reaches a turbulent state quite similar to the non-trapping run, and to FLD, though the velocity dispersions are stronger than with FLD.

We finally illustrate, in Fig. 13, the relative contributions to the average Eddington ratio  $f_{E,V}$  (grey) from the free-streaming photon flux,  $\frac{\kappa_{R,\rho} F_y}{c}$  (red) and from the trapped photon diffusion pressure  $\frac{1}{3}\nabla E_t$  (blue). As suggested by the previous plots, the diffusion

pressure dominates strongly during the first few  $t_*$ , but is more or less negligible for the remainder of the run.

Summarizing this final test, we repeated with RAMSES-RT the gas levitation experiment described in D14, in which FLD and VET closures were used for solving the moment equations of RT. We ran the same setup as described therein, modulo differences in the initial and boundary conditions required by the different methods. With FLD, the bottom boundary condition requires that

$$\frac{c\lambda}{\kappa_{R\rho}} \frac{\partial E}{\partial y} = F_*, \quad (90)$$

where  $\lambda$  is the flux-limiter that limits the speed of radiation transport to the speed of light. With VET, the comoving radiation flux in the bottom boundary ghost zone is set to  $F_y = F_*$  which is quite similar to the boundary condition we apply with M1, but they also add a ‘diffusion limit’ correction to the flux, enhancing it according to the optical thickness of the layer of cells just above the boundary. We need not apply any such correction, since the trapping of photons automatically takes care of the diffusion limit. However, the similar early evolution suggests that the correction made in VET is valid, and that the diffusion limit is indeed mostly relevant in the very bottom layer of gas cells.

All in all, our results using the M1 closure agree well with the other closures, though they are qualitatively more similar to FLD than VET: while both M1 and FLD manage to build up, after  $50t_*$ , a quasi-hydrostatic extended gas layer, VET still continues to evacuate gas at a significant rate. In light of this, since the M1 closure does not follow the gradient of radiation energy as the FLD closure does, the difference between the fate of the gas with different closures is likely to have a more nuanced explanation than just the FLD closure tending to magnify radiative Rayleigh–Taylor instabilities. It is non-trivial to read much in terms of physics into those differences, especially since it remains to be seen how far the gas can levitate with VET before reaching a turbulent equilibrium state, and whether this state eventually resembles the results with FLD and M1.

While we cannot point out specifics in the other implementations which could affect the experiment results, we can point out two factors which might affect our own results. One is the reduced speed of light. While our convergence tests that change the speed of light by a factor of a few in each direction give very similar results, it is possible that the results would be quite different if we used the real speed of light, or a value close to it. Indeed we have seen that the early acceleration of the gas is quite sensitive to the speed of light, so is likely the relatively strong deceleration, and the same may indeed apply later in the experiment. Possibly the gas can spontaneously form a coherent layer that efficiently traps the radiation. In such a scenario, the radiation builds up faster with an increasing speed of light, and with a low speed of light the trapping layer of gas may be destroyed by gravity ahead of the radiation build-up, essentially keeping the gas from being lifted. Another factor is the limitation of the M1 closure in dealing with multiple sources. In the case of efficient trapping, the radiation essentially bounces between the gas layer and the bottom of the box, and in such a case the M1 closure may create an overtly diffusive radiation field that tends to blow holes in the trapping layer of gas.

There are also limitations to the setup of this experiment, which ultimately are probably more severe than the implementation details mentioned, e.g. the lack of resolution in the initial setup, the close competition between gravity and radiation, the monogroup approach, and the lack of a third dimension.

In conclusion, and regardless of the physical limitations, this last test gives support in favour of the robustness of the new additions to RAMSES-RT, as we test all the new aspects of the code, i.e. radiation pressure, radiation–temperature coupling, radiation trapping, and relativistic corrections (though the last factor turns out to have no effect on the results). The results using RAMSES-RT are very similar to those obtained by FLD and VET in terms of the evolution of the Eddington ratio between the forces of radiation and gravity, the volume-averaged optical depth, and the ratio between the flux averaged and volume-averaged optical depths. The early acceleration of the gas is quite similar to the VET case, but instead of continuing to lift, the gas drops back to the bottom and reaches a turbulent equilibrium state, with velocity dispersions in-between those of FLD and VET.

## 4 CONCLUSIONS

We have presented several important modifications to the RHD implementation in RAMSES-RT. Previously, as described in R13, the implementation focused on the interaction of photons and gas via photoionization and the associated gas heating. In the current work, three features were added.

- (i) Multiscattered IR radiation, which is coupled to the evolution of the gas/dust temperature. A vital ingredient here is the novel treatment of radiation diffusion in a medium where the mean free path is unresolved, by partitioning the radiation into subgroups of *trapped* and *streaming* photons. In the optically thick limit, the method accurately reproduces the results of FLD, but has the great advantage over FLD that free-streaming photons are much more accurately modelled, and that photons can ‘adaptively’ alternate between trapped and free-streaming, depending on the local properties of the gas.
- (ii) Relativistic  $v/c$  corrections to the implementation of dust-coupled radiation, accounting for Doppler effects and hence the work done by the radiation on the gas.
- (iii) Momentum transfer from radiation to gas, allowing for realistic modelling of the effects of radiation pressure, both direct pressure from ionizing radiation, and from reprocessed multiscattered radiation.

We used a series of test to validate our new additions. These included a morphological assessment of a radiation field produced by the M1 closure around a galaxy disc (Section 3.1), a test of dust-absorbed radiation in a homogeneous optically semithick medium, where we compared to a full RT solution (Section 3.2), tests of direct ionizing radiation pressure in an initially homogeneous gas around a luminous young stellar population (Section 3.3), a qualitative resolution convergence test for photon trapping in a resolved versus unresolved optically thick gas (Section 3.4), quantitative tests of radiation diffusion in optically thick gas, with a radiation flash in 2D (Section 3.5), and a constant radiation source in 3D (Section 3.6), and, finally, a 2D test of the competition of gravity and multiscattering IR radiation where we compared our results in terms of average optical depths, Eddington ratios, bulk gas velocities, and turbulence, against previously published results with the ATHENA code, from D14. With the tests, we can demonstrate a robust treatment in RAMSES-RT of the interaction of radiation and gas via photoionization heating, direct pressure from ionizing radiation, dust heating, and momentum deposition by multiscattering photons.

There are limitations to the RHD approach that we use in RAMSES-RT. As discussed in both this work and R13, the M1 moment method which we employ has problems in dealing with situations of



overlapping radiation from different sources, especially in between those sources. We have presented demonstrations of this particular limitation, but we argue that even if the radiation is not always propagated to full quantitative precision, it is qualitatively robust, and generally adequate in relevant astrophysical scenarios. Another limitation of the code is that while it does offer a multifrequency approach, it is quite crude, with only a handful of frequency bins realistically attainable in standard simulations. However, (Mirocha et al. 2012) have shown that as few as four bins of (ionizing) radiation, if optimally placed in the frequency range, can eliminate frequency resolution errors to high precision, and other factors, such as resolution, likely become more limiting in studying the effects of radiation feedback on galaxy evolution.

We will follow up on this work with RHD simulations to study the effects of radiation feedback from stars and AGN on galaxy evolution, morphology, and outflows, on cosmological, galactic, and ISM scales.

The RAMSES-RT implementation, including all the new features described here, is publicly available, as a part of the RAMSES code.<sup>15</sup>

## ACKNOWLEDGEMENTS

We thank Oscar Agertz, Jeremy Blaizot, Benoit Commerçon, Yohan Dubois, and Yan-Fei Jiang for helpful discussions. Special thanks go to Shane Davis and Matthias Gonzalez for kindly sharing data and information, to Joop Schaye for many suggestions and corrections to the manuscript, and the referee, John Wise, for constructive comments. We acknowledge the organizers and participants of the workshop *Gravity's Loyal Opposition*, held at KITP in Santa Barbara 2014 April 14–July 3, at which many components of this work came together. The work was funded by the European Research Council under the European Unions Seventh Framework Programme (FP7/2007-2013)/ERC Grant agreement 278594-GasAroundGalaxies, and the Marie Curie Training Network CosmoComp (PITN-GA-2009-238356). The simulations were mostly performed using the DiRAC Data Centric system at Durham University, operated by the Institute for Computational Cosmology on behalf of the STFC DiRAC HPC Facility ([www.dirac.ac.uk](http://www.dirac.ac.uk)). This equipment was funded by BIS National E-infrastructure capital grant ST/K00042X/1, STFC capital grant ST/H008519/1, and STFC DiRAC Operations grant ST/K003267/1 and Durham University. DiRAC is part of the National E-Infrastructure. We also used the HPC resources of CINES under the allocation 2011-c2011046642 made by GENCI (Grand Equipement National de Calcul Intensif), and computing resources at the CC-IN2P3 Computing Center (Lyon/Villeurbanne - France), a partnership between CNRS/IN2P3 and CEA/DSM/Irfu.

## REFERENCES

Agertz O., Kravtsov A. V., 2014, preprint ([arXiv: 1404.2613](https://arxiv.org/abs/1404.2613))  
 Aubert D., Teyssier R., 2008, MNRAS, 387, 295  
 Balogh M. L., Pearce F. R., Bower R. G., Kay S. T., 2001, MNRAS, 326, 1228  
 Berthon C., Charrier P., Dubroca B., 2007, J. Sci. Comput., 31, 347  
 Booth C. M., Agertz O., Kravtsov A. V., Gnedin N. Y., 2013, AJ, 777, L16  
 Bouchut F., 2004, Nonlinear Stability of Finite Volume Methods for Hyperbolic Conservation Laws: And Well-Balanced Schemes for Sources. Springer-Verlag, Berlin

Brook C. B., Stinson G., Gibson B. K., Wadsley J., Quinn T., 2012, MNRAS, 424, 1275  
 Ceverino D., Klypin A., Klimek E. S., Trujillo-Gomez S., Churchill C. W., Primack J., Dekel A., 2014, MNRAS, 442, 1545  
 Commerçon B., Teyssier R., Audit E., Hennebelle P., Chabrier G., 2011, A&A, 529, 35  
 Commerçon B., Debout V., Teyssier R., 2014, A&A, 563, 11  
 Creasey P., Theuns T., Bower R. G., Lacey C. G., 2011, MNRAS, 415, 3706  
 Dalla Vecchia C., Schaye J., 2012, MNRAS, 426, 140  
 Davis S. W., Jiang Y.-F., Stone J. M., Murray N., 2014, ApJ, 796, 107 (D14)  
 Draine B. T., Li A., 2007, ApJ, 657, 810  
 Gayley K. G., Owocki S. P., Crammer S. R., 1995, ApJ, 442, 296  
 González M., Audit E., Huynh P., 2007, A&A, 464, 429  
 Haehnelt M. G., 1995, MNRAS, 273, 249  
 Hanasz M., Lesch H., Naab T., Gawryszczak A., Kowalik K., Wóltański D., 2013, AJ, 777, L38  
 Hopkins P. F., Kereš D., Oñorbe J., Faucher-Giguère C.-A., Quataert E., Murray N., Bullock J. S., 2014, MNRAS, 445, 581  
 Jiang Y.-F., Stone J. M., Davis S. W., 2012, ApJS, 199, 14  
 Keller B. W., Wadsley J., Benincasa S. M., Couchman H. M. P., 2014, MNRAS, 442, 3013  
 Krumholz M. R., Matzner C. D., 2009, ApJ, 703, 1352  
 Krumholz M. R., Thompson T. A., 2013, MNRAS, 434, 2329 (KT13)  
 Krumholz M. R., Klein R. I., McKee C. F., 2011, ApJ, 740, 74  
 Levermore C. D., 1984, J. Quant. Spectrosc. Radiat. Transfer, 31, 149  
 Liebendörfer M., Whitehouse S. C., Fischer T., 2009, ApJ, 698, 1174  
 Liu T.-P., 1987, Commun. Math. Phys., 108, 153  
 Lopez L. A., Krumholz M. R., Bolatto A. D., Prochaska J. X., Ramirez-Ruiz E., Castro D., 2014, ApJ, 795, 121  
 Mihalas D., Mihalas B. W., 1984, Foundations of Radiation Hydrodynamics. Oxford Univ. Press, New York  
 Mirocha J., Skory S., Burns J. O., Wise J. H., 2012, ApJ, 756, 94  
 Murray N., Quataert E., Thompson T. A., 2005, ApJ, 618, 569  
 Murray N., Quataert E., Thompson T. A., 2010, ApJ, 709, 191  
 Norman M. L., Reynolds D. R., So G. C., Harkness R. P., Wise J. H., 2015, ApJS, 216, 16  
 Oppenheimer B. D., Davé R., 2006, MNRAS, 373, 1265  
 Pawlik A. H., Schaye J., 2009, MNRAS, 396, L46  
 Pawlik A. H., Schaye J., 2011, MNRAS, 412, 1943  
 Petkova M., Springel V., 2009, MNRAS, 396, 1383  
 Pfrommer C., Enßlin T. A., Springel V., Jubelgas M., Dolag K., 2007, MNRAS, 378, 385  
 Rosdahl J., Blaizot J., Aubert D., Stranex T., Teyssier R., 2013, MNRAS, 436, 2188 (R13)  
 Salem M., Bryan G. L., 2014, MNRAS, 437, 3312  
 Sales L. V., Marinacci F., Springel V., Petkova M., 2014, MNRAS, 439, 2990  
 Scannapieco C. et al., 2012, MNRAS, 423, 1726  
 Schaye J. et al., 2015, MNRAS, 446, 521  
 Semenov D., Henning T., Helling C., Ilgner M., Sedlmayr E., 2003, A&A, 410, 611  
 Skinner M. A., Ostriker E. C., 2013, ApJS, 206, 21  
 Sugihara T., Ostriker J. P., 1998, ApJ, 507, 16  
 Teyssier R., 2002, A&A, 385, 337  
 Thompson T. A., Fabian A. C., Quataert E., Murray N., 2015, MNRAS, 449, 147  
 Wise J. H., Abel T., 2011, MNRAS, 414, 3458  
 Wise J. H., Abel T., Turk M. J., Norman M. L., Smith B. D., 2012, MNRAS, 427, 311

## APPENDIX A: RELATIVISTIC CORRECTIONS TO THE RHD EQUATIONS

We describe briefly the RHD equations, taking into account  $v/c$  terms that were missing in this paper so far, which represent relativistic Doppler effects between the rest frames of the gas and the

<sup>15</sup> <https://bitbucket.org/rteyssi/ramses>

radiation. These equations are derived from the classical textbook on RHD, Mihalas & Mihalas (1984).

We now distinguish between the radiation energy expressed in the gas comoving frame, noted  $E_0$ , from the radiation energy in the lab frame, noted  $E$  in the main text. We also define the radiation flux vector in the comoving frame as  $F_0$ , and the lab frame radiation flux  $F$ . The gas total energy is defined as usual by

$$E_{\text{gas}} = \frac{1}{2}\rho v^2 + e, \quad (\text{A1})$$

where we recall  $\rho$  and  $v$  are the gas density and speed, respectively, and  $e$  is the gas internal thermal energy.

We now add  $v/c$  terms to the radiation momentum equations (8) and (9), neglecting only  $(v/c)^2$  terms (see Mihalas & Mihalas 1984, page 423).

$$\frac{\partial E}{\partial t} + \nabla \cdot \mathbf{F} = \kappa\rho \left( caT^4 - \tilde{c}E + \mathbf{v} \cdot \frac{1}{c}\mathbf{F} \right), \quad (\text{A2})$$

$$\frac{\partial \mathbf{F}}{\partial t} + \tilde{c}^2 \nabla \cdot \mathbf{D}E = \kappa\rho\tilde{c} \left( -\mathbf{F} + \mathbf{v}aT^4 + \mathbf{v} \cdot \frac{\tilde{c}}{c}\mathbf{D}E \right). \quad (\text{A3})$$

Note that  $\lambda = (\kappa\rho)^{-1}$  is the frequency-averaged mean free path computed in the comoving frame. Doppler effects are therefore only accounted for up to  $v/c$  in the previous explicit form, and the radiation variables are still in the lab frame. This formulation is therefore referred to as *the mixed frame equations*.

We find it convenient to re-express these equations using the comoving radiation variables, when coupled to the thermochemistry. For this, we use the Lorentz transform up to first order in  $v/c$  to compute comoving variables as a function of the lab frame variables. We have (Mihalas & Mihalas 1984, page 417):

$$E_0 = E - \frac{2}{\tilde{c}c}\mathbf{v} \cdot \mathbf{F}, \quad (\text{A4})$$

$$\mathbf{F}_0 = \mathbf{F} - \mathbf{v} \cdot \frac{\tilde{c}}{c}E(\mathbf{1} + \mathbf{D}). \quad (\text{A5})$$

Injecting these relations into the mixed frame equations (A2) and (A3) leads to the form

$$\frac{\partial E}{\partial t} + \nabla \cdot \mathbf{F} = \kappa\rho \left( caT^4 - \tilde{c}E_0 \right) - \mathbf{v} \cdot \frac{\kappa\rho}{c}\mathbf{F}, \quad (\text{A6})$$

$$\frac{\partial \mathbf{F}}{\partial t} + \tilde{c}^2 \nabla \cdot \mathbf{D}E = \kappa\rho\tilde{c}\mathbf{F}_0 + \mathbf{v} \frac{\kappa\rho\tilde{c}}{c} \left( caT^4 - \tilde{c}E \right). \quad (\text{A7})$$

The source terms are now easier to interpret: the first term on the RHS of the energy equation is the classical radiation and matter coupling term in the comoving frame. The second term is equal to minus the work of the radiation force in the lab frame. In the radiation flux equation, the first term is the radiation force in the comoving frame, while the second one is a purely relativistic term usually identified as a *frame dragging effect* between matter and radiation. The gas energy and momentum equations (11) and (12) (ignoring gravity and other heating/cooling processes) are modified accordingly and are written using a globally strictly conservative form

$$\frac{\partial E_{\text{gas}}}{\partial t} + \nabla \cdot (\mathbf{v}(E_{\text{gas}} + P)) = \kappa_P\rho (\tilde{c}E_0 - caT^4) - \mathbf{v} \cdot \frac{\kappa_P\rho}{c}\mathbf{F}, \quad (\text{A8})$$

$$\frac{\partial \rho\mathbf{v}}{\partial t} + \nabla \cdot (\rho\mathbf{v} \otimes \mathbf{v} + \mathbf{P}\mathbf{1}) = \frac{\kappa_R\rho}{c}\mathbf{F}_0 - \mathbf{v} \frac{\kappa_R\rho}{c^2} (caT^4 - \tilde{c}E). \quad (\text{A9})$$

We directly exploit this form of the RHD equations in our numerical implementation, by adding each contribution in a classical operator splitting approach.

## APPENDIX B: TRAPPED VERSUS STREAMING PHOTONS IN A MIXED FRAME FRAMEWORK

In order to deal with extremely opaque conditions, for which the mean free path,  $\lambda_R = (\kappa_R\rho)^{-1}$ , is much smaller than the grid spacing  $\Delta x$ , we have developed in Section 2.4.2 a trapped/streaming radiation approach that properly captures the diffusion limit, even if one does not resolve the mean free path. This method was presented without taking into account the relativistic corrections discussed in the previous section. We now consider both the comoving and the lab frame, and our trapped photons are assumed to be isotropic *in the comoving frame*. This means that  $\mathbf{F}_t^0 = 0$  and, to first order in  $v/c$ , one has from equations (A4) and (A5):

$$E_t = E_t^0, \quad \mathbf{P}_t = \frac{E_t^0}{3}\mathbf{1} \quad \text{and} \quad \mathbf{F}_t = \frac{4}{3}\frac{\tilde{c}}{c}E_t^0\mathbf{v}, \quad (\text{B1})$$

where we now express the comoving variables with a ‘0’ superscript rather than a subscript. We split the radiation energy into trapped and streaming components  $E = E_t^0 + E_s$ , using the decomposition of Section 2.4.2 based on the local cell optical depth. The total radiation energy equation (equation 35, ignoring the  $\dot{E}$  source term) then becomes

$$\begin{aligned} \frac{\partial E_t^0}{\partial t} + \frac{\partial E_s}{\partial t} + \nabla \cdot \left( \mathbf{F}_s + \frac{4}{3}\frac{\tilde{c}}{c}E_t^0\mathbf{v} \right) \\ = \kappa_P\rho \left( caT^4 - \tilde{c}E_t^0 - \tilde{c}E_s \right) - \mathbf{v} \cdot \frac{\kappa_P\rho}{c}\mathbf{F}, \end{aligned} \quad (\text{B2})$$

and the total radiation flux equation (equation 36) becomes

$$\begin{aligned} \frac{\partial \mathbf{F}_s}{\partial t} + \frac{\tilde{c}^2}{3}\nabla E_t^0 + \tilde{c}^2 \nabla \cdot (\mathbf{D}E_s) \\ = -\kappa_R\rho\tilde{c}\mathbf{F}_s^0 + \mathbf{v} \frac{\kappa_R\rho\tilde{c}}{c} \left( caT^4 - \tilde{c}E \right). \end{aligned} \quad (\text{B3})$$

In the diffusion regime, we would like to recover equation (40) in the comoving frame, i.e.

$$\mathbf{F}_s^0 \simeq -\frac{\tilde{c}\lambda_R}{3}\nabla E_t^0. \quad (\text{B4})$$

In order to enforce our scheme to satisfy this limit when the cell size is large compared to the mean free path, we exploit our GLF flux function (equation 17) and we fix the streaming to trapped photon ratio by

$$E_t^0 = \frac{3\tau_c}{2}E_s. \quad (\text{B5})$$

We then solve for the streaming photon energy and flux variables in equations (B2) and (B3) using our mixed frame M1 Godunov solver

$$\frac{\partial E_s}{\partial t} + \nabla \cdot \mathbf{F}_s = -\kappa_P\rho\tilde{c}E_s^0 - \mathbf{v} \cdot \frac{\kappa_P\rho}{c}\mathbf{F}_s, \quad (\text{B6})$$

$$\frac{\partial \mathbf{F}_s}{\partial t} + \tilde{c}^2 \nabla \cdot \mathbf{D}E_s = -\kappa_R\rho\tilde{c}\mathbf{F}_s^0 + \mathbf{v} \frac{\kappa_R\rho\tilde{c}}{c} \left( caT^4 - \tilde{c}E \right). \quad (\text{B7})$$

The total radiative force is decomposed into a streaming and a trapped component as before,

$$\frac{\kappa_R\rho}{c}\mathbf{F} = \frac{\kappa_R\rho}{c}\mathbf{F}_s - \frac{1}{3}\frac{\tilde{c}}{c}\nabla E_t^0. \quad (\text{B8})$$

The work of the radiation force (with a minus sign) is decomposed between the streaming and the trapped photon energy equation. For the latter, we solve the trapped part of the radiation energy equation (B2), namely

$$\frac{\partial E_t^0}{\partial t} + \nabla \cdot \left( \frac{4}{3} \frac{\tilde{c}}{c} E_t^0 \mathbf{v} \right) = \kappa_P \rho (caT^4 - \tilde{c}E_t^0) + \mathbf{v} \cdot \frac{1}{3} \frac{\tilde{c}}{c} \nabla E_t^0, \quad (\text{B9})$$

which can be rewritten as the classical comoving radiation energy equation

$$\frac{\partial E_t^0}{\partial t} + \nabla \cdot \left( \frac{\tilde{c}}{c} E_t^0 \mathbf{v} \right) + P_{\text{rad}} \nabla \cdot \mathbf{v} = \kappa_P \rho (caT^4 - \tilde{c}E_t^0), \quad (\text{B10})$$

where the trapped radiation pressure is  $P_{\text{rad}} = \frac{1}{3} \frac{\tilde{c}}{c} E_t^0$ . The gas momentum equation (47) (ignoring the gravity term) is also modified into

$$\begin{aligned} \frac{\partial \rho \mathbf{v}}{\partial t} + \nabla \cdot [\rho \mathbf{v} \otimes \mathbf{v} + (P + P_{\text{rad}}) \mathbf{I}] \\ = \frac{\kappa_R \rho}{c} \mathbf{F}_s^0 - \mathbf{v} \cdot \frac{\kappa_P \rho}{c^2} (caT^4 - \tilde{c}E), \end{aligned} \quad (\text{B11})$$

as well as the gas total energy equation (11) (ignoring gravity and  $\Lambda$ ),

$$\begin{aligned} \frac{\partial}{\partial t} (E_{\text{gas}} + E_t^0) + \nabla \cdot [\mathbf{v}(E_{\text{gas}} + E_t^0 + P + P_t^0)] \\ = \kappa_P \rho \tilde{c} E_s^0 + \mathbf{v} \cdot \frac{\kappa_P \rho}{c} \mathbf{F}_s. \end{aligned} \quad (\text{B12})$$

We now see quite clearly that in very optically thick regions, where  $E_s \ll E_t^0$ , the streaming photons energy and flux can both be ignored and the previous set of equations just becomes a classical HD system with two pressure and energy components (gas and trapped radiation), that can be solved with a multifluid Godunov scheme. We incorporate the trapped energy radiation energy and pressure into all components of the fluid solver, as in Commerçon et al. (2011).

## APPENDIX C: A FULL RT SOLVER

In Section 3.2 we compare RAMSES-RT results to a full RT calculation, which we will now describe.

The full RT solver takes a ‘bulldozer’ approach in solving the full RT equation (1), in the four-dimensional space  $(x, y, \phi, \theta)$ , where the first two dimensions are location and the latter two are the standard solid angle, with  $\phi$  the angle from the  $x$ -axis in the  $xy$ -plane and  $\theta$  the angle from the normal vector to the  $xy$ -plane. The four-dimensional space is discretized into a four-dimensional grid  $(i, j, k, \ell)$ , with a total number of elements  $N_x \times N_y \times N_\phi \times N_\theta$ , where the  $N$ s denote the number of bins in each dimension. Each grid element contains the radiation specific intensity  $I(i, j, k, \ell)$  (in a single group approach). The radiation energy density (energy per unit volume) in a cell  $(i, j)$  is retrieved by summing the specific intensity over all angles:

$$E(i, j) = \frac{1}{c} \sum_{k=1}^{N_\phi} \sum_{\ell=1}^{N_\theta} I(i, j, k, \ell) \sin \theta \Delta \theta \Delta \phi, \quad (\text{C1})$$

where

$$\Delta \phi = \frac{2\pi}{N_\phi} \quad (\text{C2})$$

$$\Delta \theta = \frac{\pi}{N_\theta}, \quad (\text{C3})$$

$$\phi(k) = (k - 1.)\Delta \phi, \quad (\text{C4})$$

$$\theta(\ell) = (\ell - 0.5)\Delta \theta. \quad (\text{C5})$$

The specific intensity is integrated on the whole grid, according to equation (1), in discretized time-steps of length  $\Delta t = 0.5 \frac{\Delta x}{c}$ . In each time-step, the specific intensity is updated from  $I$  to  $I' + \Delta t$  in three operator-split steps: injection, advection, and scattering, which are performed as follows.

### C1 Injection

This step corresponds to solving equation (1) with only the first term on the RHS, i.e.

$$\frac{1}{c} \frac{\partial I}{\partial t} = \eta. \quad (\text{C6})$$

Here, photons are simply added to  $I(i, j, k, \ell)$  where appropriate.

In our Section 3.2 test, no such injection inside the box boundaries is in fact needed. Here, it suffices to initialize the boundary conditions such that the correct flux is emitted from the left-hand side. For all but the left boundary, the ghost cells, i.e. static cells just outside the box boundary, are initialized to zero radiation intensity, while for the left-hand side ghost cells we set

$$I(0, j, 1, \ell) = \frac{1}{2} \frac{F_*}{\sin \theta \Delta \phi \Delta \theta}, \quad (\text{C7})$$

for  $j = (1, \dots, N_y)$  and  $\ell = (N_\theta/2 - 1, N_\theta/2)$ , assuming even  $N_\theta$ .

### C2 Advection

Here, we solve equation (1) over  $\Delta t$  with only the advection term, i.e.

$$\frac{1}{c} \frac{\partial I}{\partial t} + \mathbf{n} \cdot \nabla I = 0. \quad (\text{C8})$$

First, fluxes are calculated across each intercell boundary inside the grid (and at the grid boundaries). The  $x$ -fluxes are

$$f_x \left( i + \frac{1}{2}, j, k, \ell \right) = cn_x I_\downarrow \left( i + \frac{1}{2}, j, k, \ell \right), \quad (\text{C9})$$

where  $n_x = \cos \phi \sin \theta$ , and  $I_\downarrow$  is the downstream radiation intensity, i.e.

$$I_\downarrow \left( i + \frac{1}{2}, j, k, \ell \right) = \begin{cases} I(i, j, k, \ell) & \text{if } n_x > 0, \\ I(i + 1, j, k, \ell), & \text{otherwise.} \end{cases}$$

Likewise, the  $y$ -intercell fluxes are

$$f_y \left( i, j + \frac{1}{2}, k, \ell \right) = cn_y I_\downarrow \left( i, j + \frac{1}{2}, k, \ell \right), \quad (\text{C10})$$

where  $n_y = \sin \phi \sin \theta$ , and

$$I_\downarrow \left( i, j + \frac{1}{2}, k, \ell \right) = \begin{cases} I(i, j, k, \ell) & \text{if } n_y > 0, \\ I(i, j + 1, k, \ell), & \text{otherwise.} \end{cases}$$

The radiation is then explicitly advected between cells, using the intercell fluxes:

$$\begin{aligned} I'(i, j, k, \ell) = I(i, j, k, \ell) + \frac{\Delta t}{\Delta x} \\ \left[ f_x \left( i - \frac{1}{2}, j, k, \ell \right) - f_x \left( i + \frac{1}{2}, j, k, \ell \right) \right. \\ \left. + f_y \left( i, j - \frac{1}{2}, k, \ell \right) - f_y \left( i, j + \frac{1}{2}, k, \ell \right) \right], \end{aligned} \quad (\text{C11})$$

for each  $i \in (1, \dots, N_x)$ ,  $j \in (1, \dots, N_y)$ ,  $k \in (1, \dots, N_\phi)$ ,  $\ell \in (1, \dots, N_\theta)$ .

### C3 Scattering

In the final operator-split step in the full RT calculation, the radiation is scattered isotropically. First, the radiation intensity in each cell and over all angles is semi-implicitly ‘absorbed’:

$$I''(i, j, k, \ell) = \frac{I'(i, j, k, \ell)}{1 + \Delta t \rho \kappa c}. \quad (\text{C12})$$

Then these photons are emitted isotropically (i.e. scattered):

$$I^{t+\Delta t}(i, j, k, \ell) = I''(i, j, k, \ell) + \frac{f_{\text{sc}}(i, j)}{4\pi}, \quad (\text{C13})$$

where  $f_{\text{sc}}$  is the scattered flux over the time-step,

$$f_{\text{sc}}(i, j) = \sum_{k=1}^{N_\phi} \sum_{\ell=1}^{N_\theta} [I''(i, j, k, \ell) - I'(i, j, k, \ell)] \sin \theta \Delta \phi \Delta \theta. \quad (\text{C14})$$

With equation (C13), the radiation specific intensities are fully updated to time  $t + \Delta t$ , and now the sequence of operator splitting steps (C1)–(C3) can be repeated for consecutive time-steps.

This paper has been typeset from a  $\text{\TeX}/\text{\LaTeX}$  file prepared by the author.